The Astrophysical Journal Supplement Series, 192:16 (19pp), 2011 February doi:10.1088/0067-0049/192/2/16

SEVEN-YEAR *WILKINSON MICROWAVE ANISOTROPY PROBE* (*WMAP**) OBSERVATIONS: POWER SPECTRA AND *WMAP*-DERIVED PARAMETERS

D. Larson[1], J. Dunkley[2], G. Hinshaw[3], E. Komatsu[4], M. R. Nolta[5], C. L. Bennett[1], B. Gold[1], M. Halpern[6], R. S. Hill[7], N. Jarosik[8], A. Kogut[3], M. Limon[9], S. S. Meyer[10], N. Odegard[7], L. Page[8], K. M. Smith[11], D. N. Spergel[11,12], G. S. Tucker[13], J. L. Weiland[7], E. Wollack[3], and E. L. Wright[14]

[1] Department of Physics and Astronomy, The Johns Hopkins University, 3400 N. Charles Street, Baltimore, MD 21218-2686, USA; dlarson@pha.jhu.edu
[2] Astrophysics, University of Oxford, Keble Road, Oxford, OX1 3RH, UK
[3] Code 665, NASA/Goddard Space Flight Center, Greenbelt, MD 20771, USA
[4] Department of Astronomy, University of Texas, Austin, 2511 Speedway, RLM 15.306, Austin, TX 78712, USA
[5] Canadian Institute for Theoretical Astrophysics, 60 St. George Street, University of Toronto, Toronto, ON M5S 3H8, Canada
[6] Department of Physics and Astronomy, University of British Columbia, Vancouver, BC V6T 1Z1, Canada
[7] ADNET Systems, Inc., 7515 Mission Dr., Suite A100 Lanham, MD 20706, USA
[8] Department of Physics, Jadwin Hall, Princeton University, Princeton, NJ 08544-0708, USA
[9] Columbia Astrophysics Laboratory, 550 W. 120th St., Mail Code 5247, New York, NY 10027-6902, USA
[10] Departments of Astrophysics and Physics, KICP and EFI, University of Chicago, Chicago, IL 60637, USA
[11] Department of Astrophysical Sciences, Peyton Hall, Princeton University, Princeton, NJ 08544-1001, USA
[12] Princeton Center for Theoretical Physics, Princeton University, Princeton, NJ 08544, USA
[13] Department of Physics, Brown University, 182 Hope St., Providence, RI 02912-1843, USA
[14] UCLA Physics and Astronomy, P.O. Box 951547, Los Angeles, CA 90095-1547, USA

Received 2010 January 26; accepted 2010 June 7; published 2011 January 11

ABSTRACT

The *WMAP* mission has produced sky maps from seven years of observations at L2. We present the angular power spectra derived from the seven-year maps and discuss the cosmological conclusions that can be inferred from *WMAP* data alone. With the seven-year data, the temperature (TT) spectrum measurement has a signal-to-noise ratio per multipole that exceeds unity for $l < 919$; and in band powers of width $\Delta l = 10$, the signal-to-noise ratio exceeds unity up to $l = 1060$. The third acoustic peak in the TT spectrum is now well measured by *WMAP*. In the context of a flat ΛCDM model, this improvement allows us to place tighter constraints on the matter density from *WMAP* data alone, $\Omega_m h^2 = 0.1334^{+0.0056}_{-0.0055}$, and on the epoch of matter-radiation equality, $z_{\rm eq} = 3196^{+134}_{-133}$. The temperature-polarization (TE) spectrum is detected in the seven-year data with a significance of 20σ, compared to 13σ with the five-year data. We now detect the second dip in the TE spectrum near $l \sim 450$ with high confidence. The TB and EB spectra remain consistent with zero, thus demonstrating low systematic errors and foreground residuals in the data. The low-l EE spectrum, a measure of the optical depth due to reionization, is detected at 5.5σ significance when averaged over $l = 2$–7: $l(l+1)C_l^{\rm EE}/(2\pi) = 0.074^{+0.034}_{-0.025}\ \mu{\rm K}^2$ (68% CL). We now detect the high-l, $24 \leqslant l \leqslant 800$, EE spectrum at over 8σ. The BB spectrum, an important probe of gravitational waves from inflation, remains consistent with zero; when averaged over $l = 2$–7, $l(l+1)C_l^{\rm BB}/(2\pi) < 0.055\ \mu{\rm K}^2$ (95% CL). The upper limit on tensor modes from polarization data alone is a factor of two lower with the seven-year data than it was using the five-year data. The data remain consistent with the simple ΛCDM model: the best-fit TT spectrum has an effective χ^2 of 1227 for 1170 degrees of freedom, with a probability to exceed of 9.6%. The allowable volume in the six-dimensional space of ΛCDM parameters has been reduced by a factor of 1.5 relative to the five-year volume, while the ΛCDM model that allows for tensor modes and a running scalar spectral index has a factor of three lower volume when fit to the seven-year data. We test the parameter recovery process for bias and find that the scalar spectral index, n_s, is biased *high*, but only by 0.09σ, while the remaining parameters are biased by $<0.15\sigma$. The improvement in the third peak measurement leads to tighter lower limits from *WMAP* on the number of relativistic degrees of freedom (e.g., neutrinos) in the early universe: $N_{\rm eff} > 2.7$ (95% CL). Also, using *WMAP* data alone, the primordial helium mass fraction is found to be $Y_{\rm He} = 0.28^{+0.14}_{-0.15}$, and with data from higher-resolution cosmic microwave background experiments included, we now establish the existence of pre-stellar helium at $>3\sigma$. These new *WMAP* measurements provide important tests of big bang cosmology.

Key words: cosmic background radiation – cosmological parameters – cosmology: observations – dark matter – early universe – space vehicles: instruments

1. INTRODUCTION

The *Wilkinson Microwave Anisotropy Probe* (*WMAP*; Bennett et al. 2003a, 2003b) is a Medium-Class Explorer (MIDEX) satellite aimed at understanding cosmology through full-sky observations of the cosmic microwave background (CMB). The *WMAP* full-sky maps of the temperature and polarization anisotropy in five frequency bands provide our most accurate view to date of conditions in the early universe. The *WMAP* instrument is composed of 10 differencing assemblies (DAs) spanning five frequencies from 23 to 94 GHz (Bennett et al. 2003b): one DA each at 23 GHz (K1) and 33 GHz (Ka1), two each at 41 GHz (Q1,Q2) and 61 GHz (V1,V2), and four at 94 GHz (W1–W4). Each DA is formed from two differential radiometers which are sensitive to orthogonal linear polarization modes; *WMAP* measures both temperature and polarization at each frequency. The multi-frequency data facilitate the separation of the CMB signal from foreground emission arising both from our Galaxy and from extragalactic sources. The CMB

* *WMAP* is the result of a partnership between Princeton University and NASA's Goddard Space Flight Center. Scientific guidance is provided by the *WMAP* Science Team.

angular power spectrum derived from these maps exhibits a highly coherent acoustic peak structure which makes it possible to extract a wealth of information about the composition and history of the universe, as well as the processes that seeded the fluctuations.

With accurate measurements of the first few peaks in the angular power spectrum, CMB data have enabled the following advances in our understanding of cosmology (Spergel et al. 2003, 2007; Dunkley et al. 2009; Komatsu et al. 2009): the dark matter must be non-baryonic and interact only weakly with atoms and radiation; the density of atoms in the universe is known to 3% and accords well with big bang nucleosynthesis (BBN); the measured acoustic scale at $z = 1090$, combined with the local distance scale and baryon acoustic oscillation (BAO) data, demonstrates that the universe is spatially flat, to within 1%; the Hubble constant is determined to 3% using only acoustic fluctuation data (CMB+BAO), and it accords well with local measurements; the primordial fluctuations are adiabatic and Gaussian, and the spectrum is slightly tilted.

The statistical properties of the CMB fluctuations measured by *WMAP* are close to Gaussian with random phase (Komatsu et al. 2003, 2009; Spergel et al. 2007). There are several hints of possible deviations from this case as discussed in Bennett et al. (2011) and Komatsu et al. (2011). If the fluctuations are Gaussian and random phase, then their statistical information content is completely determined by the angular power spectra of the sky maps.

This paper derives the angular power spectra from the *WMAP* seven-year sky maps and presents the cosmological parameters that can be determined from them. The new results improve upon previous results in many ways: additional data reduce the random noise, which is especially important for studying the temperature signal on small angular scales and the polarization signal on large angular scales; *W*-band data are now incorporated in the TE spectrum measurement to improve precision; new simulations have been carried out to test the accuracy of parameter recovery and to test a model's goodness of fit. The result is the most accurate full-sky measurement to date of CMB anisotropy down to an angular scale of $\sim 0.^{\circ}25$.

This paper is one of six that accompany the seven-year *WMAP* data release. Jarosik et al. (2011) discuss the seven-year map-making process, systematic error limits, and basic results. Gold et al. (2011) discuss galactic foreground emission, and its removal in seven-year data. Bennett et al. (2011) discuss possible anomalies in the *WMAP* CMB maps. Komatsu et al. (2011) discuss the interpretation of the *WMAP* data, in combination with other relevant cosmological data. Weiland et al. (2011) discuss the *WMAP* measurements of the outer planets and selected bright sources for use as microwave calibrators.

The layout of this paper is as follows. In Section 2, we present the *WMAP* seven-year power spectra. In Section 3, we discuss simulations that were performed to test for bias in our cosmological parameter fits. In Section 4, we discuss cosmological conclusions that can be drawn from *WMAP* data alone, and in Section 5 we discuss the goodness of fit of the six parameter ΛCDM theory. We conclude in Section 6.

2. SEVEN-YEAR POWER SPECTRA

In this section, we present the temperature and polarization power spectra derived from the seven-year sky maps and compare them to the five-year spectra.

2.1. Definitions and Methodology

Since *WMAP* measures both temperature and polarization, there are multiple power spectra to consider. On a sphere, the temperature field can be decomposed into spherical harmonics,

$$T(\hat{n}) = \sum_{l=0}^{\infty} \sum_{m=-l}^{l} a_{T,lm} Y_{lm}(\hat{n}), \tag{1}$$

where $\hat{n}$ is a unit direction vector and a_T refers specifically to the temperature field. Likewise, the Q and U Stokes parameters for linear polarization can be decomposed into complex spin-2 harmonics (Newman & Penrose 1966; Goldberg et al. 1967),

$$Q(\hat{n}) + iU(\hat{n}) = \sum_{l=2}^{\infty} \sum_{m=-l}^{l} a_{2,lm}\, {}_2Y_{lm}(\hat{n}). \tag{2}$$

The spin-2 coefficients can then be combined to represent polarization modes that have no curl (E modes) and modes that have no divergence (B modes). These are given by the coefficients (Zaldarriaga & Seljak 1997; Larson 2006),

$$a_{E,lm} = -\frac{a_{2,lm} + (-1)^m a^*_{2,l\,-m}}{2} \tag{3}$$

$$a_{B,lm} = -\frac{a_{2,lm} - (-1)^m a^*_{2,l\,-m}}{2i} \tag{4}$$

(Kamionkowski et al. 1997 use an alternative approach.) The angular power spectra are related to these modes according to

$$C_l^{XY} = \frac{1}{2l+1} \sum_{m=-l}^{l} a_{X,lm} a^*_{Y,lm} \tag{5}$$

where X, $Y = T$, E, or B. The data are currently consistent with being isotropic and Gaussian distributed, but this condition should continue to be tested (Bennett et al. 2011).

There are six independent power spectra that can be constructed from the temperature and polarization data, TT, TE, TB, EE, EB, and BB, though in theories in which parity is conserved, TB and EB are expected to be zero. In general, foreground signals (and systematic effects) can produce non-zero TB, EB, and BB so these spectra provide a good test for residual polarization contamination.

For the seven-year analysis, we use the same combination of estimators that were used with the five-year data (Nolta et al. 2009). This combination is a trade-off between statistical accuracy and computational speed. We present new tests of the accuracy of the likelihood function constructed from these estimators in Section 3. To summarize the combination: for low-l TT ($\leqslant 32$) we compute the likelihood of a model directly from the seven-year Internal Linear Combination (ILC) maps (Gold et al. 2011). For high-l ($l > 32$) TT, we use the MASTER pseudo-C_l quadratic estimator (Hivon et al. 2002). For low-l polarization, $l \leqslant 23$ TE, EE, and BB, we use the pixel-space estimator described in Page et al. (2007), and for high-l TE ($l > 23$) we use the MASTER quadratic estimator.

2.2. Changes Affecting the Seven-year Spectra

Several data processing and analysis changes were applied to the seven-year data which resulted in improvements beyond those which would be expected from additional integration time.

2.2.1. Map Making with Asymmetric Masking

A new map-making technique was adopted for the seven-year data which combines optimal noise handling with "asymmetric" data masking (Jarosik et al. 2011). With this change, certain regions in the seven-year maps employ more data samples than they would have with the previous pipeline. These "Galactic echo" regions are thus more sensitive than a simple five-year to seven-year integration time scaling would predict.

2.2.2. Multipole Range

The additional sensitivity afforded by more data has made it possible to extend the usable multipole range in the power spectra and likelihood code. For the TT data, we extend the upper multipole limit, $l_{\rm max}$, from 1000 to 1200. For the TE spectrum, we have determined that high-l W-band polarization data are sufficiently free from systematic effects that they can be employed in the TE spectrum estimate (Jarosik et al. 2011). This significantly improves the sensitivity in the seven-year TE spectrum and allows us to extend the TE multipole limit from 450 to 800.

2.2.3. Mask and f_{sky}

The seven-year sky masks have been augmented slightly using a χ^2 analysis of the Q – V and V – W difference maps, *after* the normal template cleaning had been applied (Jarosik et al. 2011; Gold et al. 2011). This results in a slightly more conservative mask which decreases the unmasked sky fraction by ∼3% (from 81.7% to 78.3% for the KQ85 cut—the new cut is denoted KQ85y7). Given the χ^2 threshold applied during the construction of the extended mask, residual foreground signals outside the mask are essentially undetectable on the scale of the instrument noise in a ∼2° pixel, so the data are fractionally more robust to foreground contamination.

The power spectrum sensitivity depends on sky cut according to $\Delta C_l \propto f_{\rm sky}^{-1}$ where $f_{\rm sky}$ is (approximately) the fraction of sky that survives the cut (Hinshaw et al. 2003; Verde et al. 2003). In practice, $f_{\rm sky}$ is a function of l that is calibrated with simulations, so there is a different constant of proportionality at each l, but it scales with the fraction of usable sky area. Thus, the increased sky mask results in a slight loss of sensitivity in the TT spectrum for $l \lesssim 550$, where the spectrum is sky variance limited.

For the TE spectrum, we have generated new simulations to test the calibration of $f_{\rm sky,TE}$ which enters into the error propagation from sky maps to spectra. The mean χ^2 deduced from our simulations was 760 for spectra with 777 degrees of freedom, a factor of 1.022 too low, indicating that our previous TE error estimate was a factor of 1.011 too high. Therefore, we have scaled $f_{\rm sky,TE}$ by 1.011 to produce a unit mean χ^2 per degree of freedom, following the precedent used to calibrate $f_{\rm sky,TT}$ from simulations (Verde et al. 2003). In Section 5, we present the TE χ^2 of the seven-year flight data and conclude that the ΛCDM model fits the TE data well.

2.3. Temperature (TT) Spectrum

For $l \leqslant 32$, the spectrum is obtained using a Blackwell–Rao estimator applied to a chain of Gibbs samples (Wandelt et al. 2004; Jewell et al. 2004; Chu et al. 2005; Dunkley et al. 2009) based on the seven-year ILC map and the KQ85y7 mask. The specifications used to sample the map are described in Dunkley et al. (2009). For $l > 32$, the spectrum was derived from the MASTER pseudo-C_l quadratic estimator applied to the seven-year, template-cleaned V- and W-band maps (Gold et al. 2011). (The MASTER spectrum is technically derived from $l = 2$ to 1200, then the $l = 2$–32 portion is discarded, but correlations induced by mode coupling are retained for $l > 32$.) The pseudo-a_{lm} coefficients were computed from the $N_{\rm side} = 1024$ maps for each single year and each single DA, V1-W4. For $l < 600$, the coefficients were evaluated with uniform pixel weights, while inverse-noise weights were used for $l > 600$. (The transition was made at $l = 500$ in the five-year analysis.) As noted above, we adopt a slightly larger sky mask, denoted KQ85y7.

The pseudo-C_l cross-power spectra are computed from all off-diagonal pairs of pseudo-a_{lm} coefficients,

$$\tilde{C}_l^{(ij)} = \frac{1}{2l+1} \sum_{m=-l}^{l} \tilde{a}_{lm}^{(i)} \tilde{a}_{lm}^{*(j)}, \quad (6)$$

where i, j refer to a DA–year combination (Hinshaw et al. 2007) and the tilde indicates a pseudo-quantity (spectrum or coefficient). These component pseudo-spectra are deconvolved using the MASTER formalism[15], and the results are combined by band into VV, VW, and WW spectra for the purposes of removing the residual point source amplitude. The unresolved point source contribution to the sky continues to be treated as a power law in thermodynamic temperature, falling as $\nu^{-2.09}$ (Nolta et al. 2009), but see Colombo & Pierpaoli (2010) for an alternative approach to the spectral dependence. Using the same fitting methodology as in the five-year analysis, we find its amplitude to be $10^3 A_{\rm ps} = 9.0 \pm 0.7\,\mu{\rm K}^2$ sr, when fit to the seven-year Q-, V-, and W-band spectra evaluated with the KQ85y7 mask. (Most of the cosmological parameters reported in this paper were fit using a preliminary version of the likelihood that had a small masking error that produced a slightly biased TT spectrum at high l and a correspondingly higher residual source amplitude, which mostly compensated for the bias. We have checked that substituting the correct TT spectrum has a negligible effect on the parameter fits.) After this source model is subtracted from each band, the spectra are combined to form our best estimate of the CMB signal, shown in Figure 1.

The seven-year power spectrum is cosmic variance limited, i.e., cosmic variance exceeds the instrument noise, up to $l = 548$. (This limit is slightly model dependent and can vary by a few multipoles.) The spectrum has a signal-to-noise ratio greater than one per l-mode up to $l = 919$, and in band powers of width $\Delta l = 10$, the signal-to-noise ratio exceeds unity up to $l = 1060$. The largest improvement in the seven-year spectrum occurs at multipoles $l > 600$ where the uncertainty is still dominated by instrument noise. The instrument noise level in the seven-year spectrum is 39% smaller than with the five-year data, which makes it worthwhile to extend the *WMAP* spectrum estimate up to $l = 1200$ for the first time. See Figure 2 for a comparison of the seven-year error bars to the five-year error bars. The third acoustic peak is now well measured and the onset of the Silk damping tail is also clearly seen by *WMAP*. As we show in Section 4, this leads to a better measurement of $\Omega_m h^2$ and the epoch of matter-radiation equality, $z_{\rm eq}$, which, in turn, leads to better constraints on the effective number of relativistic species, $N_{\rm eff}$, and on the primordial helium abundance, $Y_{\rm He}$. The improved sensitivity at high l is also important for higher-resolution CMB experiments that use *WMAP* as a primary calibration source.

[15] In principle, we can obtain a modestly more sensitive spectrum estimate at intermediate multipoles by employing C^{-1} weighting in the computation of the pseudo-a_{lm}. We are currently developing such code for use in cross-power spectra with the intention of applying it to the final nine-year data.

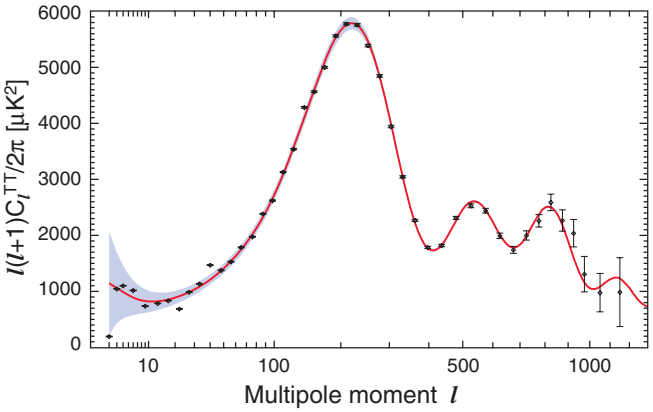

Figure 1. Seven-year temperature (TT) power spectrum from *WMAP*. The third acoustic peak and the onset of the Silk damping tail are now well measured by *WMAP*. The curve is the ΛCDM model best fit to the seven-year *WMAP* data: $\Omega_b h^2 = 0.02270$, $\Omega_c h^2 = 0.1107$, $\Omega_\Lambda = 0.738$, $\tau = 0.086$, $n_s = 0.969$, $\Delta^2_{\mathcal{R}} = 2.38 \times 10^{-9}$, and $A_{SZ} = 0.52$. The plotted errors include instrument noise, but not the small, correlated contribution due to beam and point source subtraction uncertainty. The gray band represents cosmic variance. A complete error treatment is incorporated in the *WMAP* likelihood code. The points are binned in progressively larger multipole bins with increasing l; the bin ranges are included in the seven-year data release.

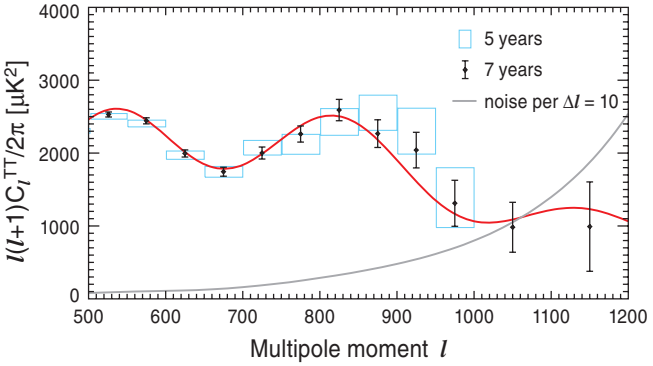

Figure 2. High-l TT spectrum measured by *WMAP*, showing the improvement with seven years of data. The points with errors use the full data set while the boxes show the five-year results with the same binning. The TT measurement is improved by >30% in the vicinity of the third acoustic peak (at $l \approx 800$), while the two bins from $l = 1000$ to 1200 are new with the seven-year data analysis.

2.4. Temperature–Polarization (TE, TB) Cross Spectra

The seven-year temperature–polarization cross-power spectra were formed using the same methodology as the five-year spectrum (Page et al. 2007; Nolta et al. 2009). For $l \leqslant 23$, the cosmological model likelihood is estimated directly from low-resolution temperature and polarization maps. The temperature input is a template-cleaned, co-added V + W-band map, while the polarization input is a template-cleaned, co-added Ka + Q + V-band map (Gold et al. 2009). In this regime, the spectrum can be inferred from the conditional likelihood of C_l values (individual or binned), but these estimates are only used for visualization.

For $l > 23$, the temperature-polarization spectra are derived using the MASTER quadratic estimator, extended to include polarization data (Page et al. 2007). (As above, the MASTER spectrum is evaluated from $l = 2$, but the result from $l = 2$–23 is discarded.) The temperature input is a template-cleaned, co-added V+W-band map, while the polarization input is a template-cleaned, co-added Q+V+W-band map. The inclusion of W-band data in the high-l TE and TB spectra is new with the seven-year data release (Jarosik et al. 2011). Since the W-band radiometers have the highest angular resolution, the inclusion of the W band significantly enhances the sensitivity of these high-l spectra.

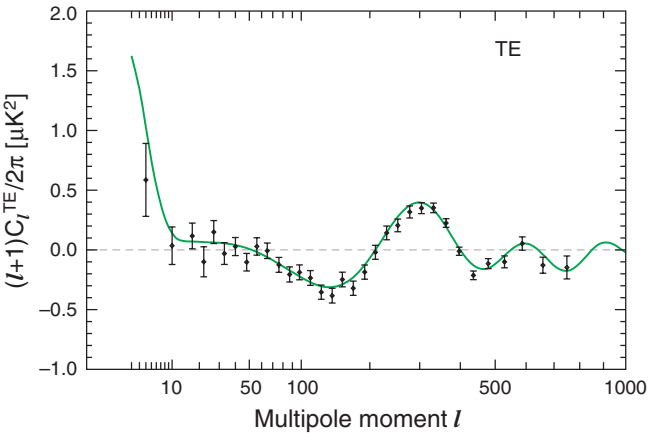

Figure 3. Seven-year temperature-polarization (TE) cross-power spectrum measured by *WMAP*. The second trough (TE < 0) in the spectrum in the vicinity of $l = 450$ is now clearly detected. The green curve is the ΛCDM model best fit to the seven-year *WMAP* data, as in Figure 1. The plotted errors depict the diagonal elements of the covariance matrix and include both cosmic variance and instrument noise. A complete error treatment is incorporated in the *WMAP* likelihood code. Note that the plotted spectrum is $(l + 1)C_l^{TE}/(2\pi)$, and not $l(l + 1)C_l^{TE}/(2\pi)$.

The seven-year TE spectrum measured by *WMAP* is shown in Figure 3. For all except the first bin, the MASTER values and their Gaussian errors are plotted. The first bin shows the conditional maximum likelihood value based on the pixel likelihood mentioned above. The slight adjustment for $f_{\rm sky,TE}$ is included in the error bars. With two additional years of integration and the inclusion of W-band data, we now detect the TE signal with a significance of 20σ, up from 13σ with the five-year data. Indeed, for $10 < l < 300$, the TE error is less than 65% of the five-year value, and for $l > 300$ the sensitivity improvement is even larger due to the W-band's finer resolution. At $l = 800$ the seven-year TE error is 36% of the five-year value. A qualitatively new feature seen in the seven-year spectrum is a second trough (TE < 0) near $l = 450$. See Figure 4 for a comparison of the seven-year to five-year error bars, for the TE and TB spectra. Overall, the TE data are quite consistent with the simplest six-parameter ΛCDM model; we discuss its goodness of fit in Section 5.

The observed TE signal is the result of a specific polarization pattern around hot and cold spots in the temperature anisotropy. In particular, the acoustic peak structure in TE corresponds to a series of concentric rings of alternating radial and tangential polarization (relative to a radial reference direction). Komatsu et al. (2011) perform a stacking analysis of the seven-year temperature and polarization maps and show that the effect is detected in the seven-year *WMAP* sky maps with a significance of 8σ.

The seven-year TB spectrum measured by *WMAP* is shown in Figure 5. In this case, because the signal-to-noise ratio is low, the MASTER points and their Gaussian errors are plotted over the full l range, including the first bin. The measured spectrum is consistent with zero: the χ^2 for the null hypothesis (TB = 0) is 793.5 for 777 degrees of freedom. The probability to exceed that amount is 33%. The absence of a detectable signal is consistent with the ΛCDM model, which predicts zero. It is also an indication that systematic errors and foreground

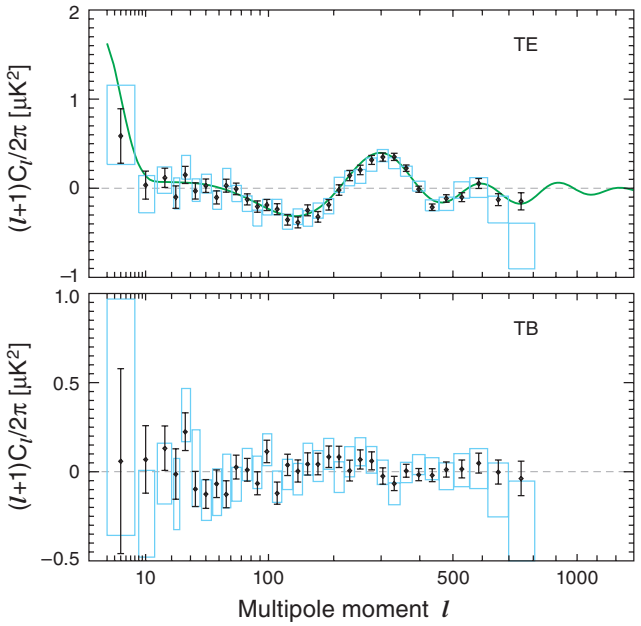

Figure 4. TE and TB high-l spectra measured by *WMAP*, showing the improvement with seven years of data. The points with errors use the full data set while the boxes show the five-year results with the same binning. The spectra are greatly improved by the addition of W-band data. The non-detection of TB signal is expected; it provides a good check of systematic errors and foreground residuals and can be also used to set limits on polarization rotation due to parity-violating effects (Section 2.4 and Komatsu et al. 2011).

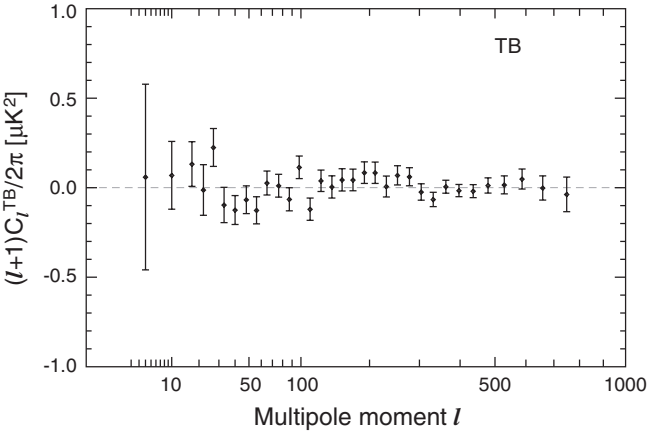

Figure 5. Seven-year temperature-polarization (TB) cross-power spectrum measured by *WMAP*. This spectrum is predicted to be zero in the basic ΛCDM model and the measured spectrum is consistent with zero. TB provides a useful null test for systematic errors and foreground residuals. Komatsu et al. (2011) use the TB and TE spectra to place an upper limit on polarization rotation due to parity-violating effects. The TB χ^2 for the null hypothesis (TB = 0) is 793.5 for 777 degrees of freedom. The probability to exceed that amount is 33%. Note that the plotted spectrum is $(l+1)C_l^{TB}/(2\pi)$, and not $l(l+1)C_l^{TB}/(2\pi)$.

contamination are not significant at the level of $\sim 0.1\,\mu\mathrm{K}^2$ in $(l+1)C_l^{TB}$.

Komatsu et al. (2011) use the seven-year TE and TB data to place limits on polarization rotation due to parity-violating effects. Polarization rotation would cause TE signal generated at the last scattering surface to transform into observed TB power. The absence of TB signal leads to an upper limit on rotation of $\Delta\alpha = -1.^\circ1 \pm 1.^\circ4(\mathrm{stat}) \pm 1.^\circ5(\mathrm{sys})$.

2.5. Polarization (EE, EB, BB) Spectra

We begin by discussing the low-l polarization spectra, and then move on to the high-l EE spectrum.

The most reliable way to estimate the low-l polarization spectra is to use the pixel-space likelihood code to generate the posterior distributions of individual (or binned) C_l values. In the seven-year data, this code is based on a co-added Ka + Q + V map. The most conservative, but costly, method is to produce a Markov Chain that allows each C_l to vary independently; the resulting distribution of any single C_l will be the marginalized distribution for that multipole moment. A Gibbs sampling technique could also be used, but this works best with a high signal-to-noise ratio. However, Gibbs sampling in lower signal-to-noise regions can be performed successfully, as shown by Jewell et al. (2009). A much more tractable approach is to compute the conditional likelihood in which the likelihood of a single C_l is evaluated while all other moments are held fixed. We adopt the latter approach to visualize the low-l EE and BB spectra. This method has also been used in previous *WMAP* papers as well as (for example) Gruppuso et al. (2009) in their verification of the five-year *WMAP* low-l spectra. In the context of parameter fitting, the estimated C_l are constrained to vary according to the model.

Figure 6 shows the conditional likelihood for the EE multipoles from $l = 2$–7 for two different reference spectra. The black curves show the likelihood of C_l^{EE} when the $C_{l'}^{EE}$ are fixed to the best-fit ΛCDM model for $l' \neq l$. The red curves are the analogous distributions when the reference spectrum is taken to be the maximum likelihood spectrum. This maximum likelihood spectrum was obtained by numerical maximization of the likelihood code for the TT, TE, EE, and BB spectra for $2 \leqslant l \leqslant 10$, a maximization in 36 dimensions, while the spectra at $l > 10$ were fixed at the best-fit ΛCDM model. Save for $l = 3$ and 6, the likelihood curves are relatively insensitive to the difference between these two reference spectra. From these curves it is clear that the majority of the statistical weight in the low-l EE detection is at $l = 4$, with $l = 2$ also contributing significant power.

A standard reionization scenario would give rise to a relatively flat spectrum in $\mathcal{C}_l^{EE} = l(l+1)C_l^{EE}/(2\pi)$ over the range $l = 2$–7, so it is of interest to evaluate the posterior distribution of a band power with constant $\mathcal{C}$ over this range. As shown in Figure 7, we find

$$\mathcal{C}_{2-7}^{EE} = 0.074^{+0.034}_{-0.025}\ \mu\mathrm{K}^2\ (68\%\ \mathrm{CL}). \quad (7)$$

This result was obtained with the pixel likelihood code, and so the error bars include cosmic variance. Additionally, a model with zero TE and EE power for $l = 2$–7 is disfavored at 5.5σ relative to the most-likely constant band power in this l range.

Figure 8 shows the conditional likelihood for the BB multipoles from $l = 2$–7 for two different reference spectra. The black curves show the likelihood of C_l^{BB} when the $C_{l'}^{BB}$ are fixed to the best-fit ΛCDM model (zero, except for small contributions from lensing) for $l' \neq l$. The red curves are the analogous distributions when the reference spectrum is taken to be the maximum likelihood spectrum for $l \leqslant 10$ and the ΛCDM spectrum (again, effectively zero) for $l > 10$. Save for $l = 2$, the posterior likelihood curves are insensitive to the reference spectrum. There is no significant detection of BB power in any single multipole in the seven-year *WMAP* data. As shown in Figure 9, we evaluate the posterior likelihood of a single constant band power from $l = 2$–7 and find it is also consistent with zero. We

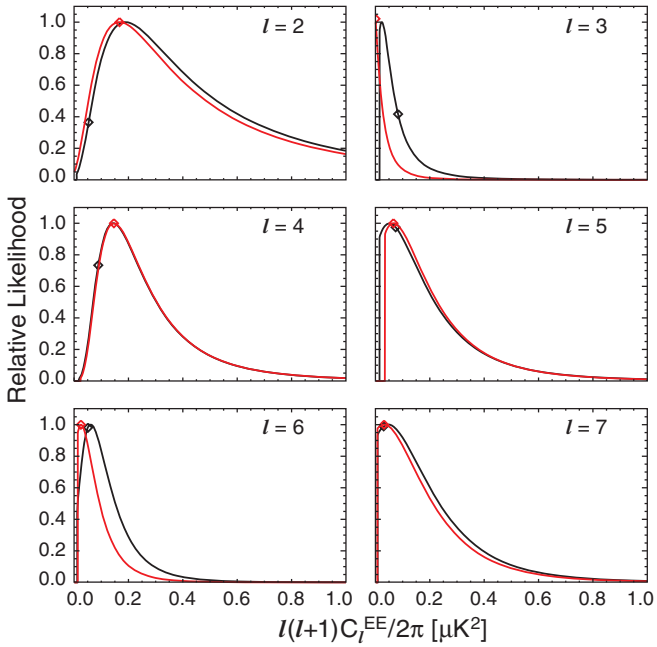

Figure 6. Conditional likelihoods of $l(l+1)C_l^{EE}/(2\pi)$ for $l = 2$–7 computed with the *WMAP* likelihood code. The Ka, Q, and V bands contribute to the low-l polarized pixel likelihood. In each panel, the black curve is the conditional likelihood for a given multipole when all other multipoles are held fixed at the value of the best-fit ΛCDM model (indicated by the black diamonds). The red curve in each panel is the conditional likelihood when all other multipoles are held fixed at the maximum likelihood value of the spectrum, indicated by the red diamonds. The maximum likelihood spectra were determined by a numerical maximization of the *WMAP* likelihood code, for $l = 2$–10, for TT, TE, EE, and BB. Points with $l > 10$ were fixed at the best-fit ΛCDM value.

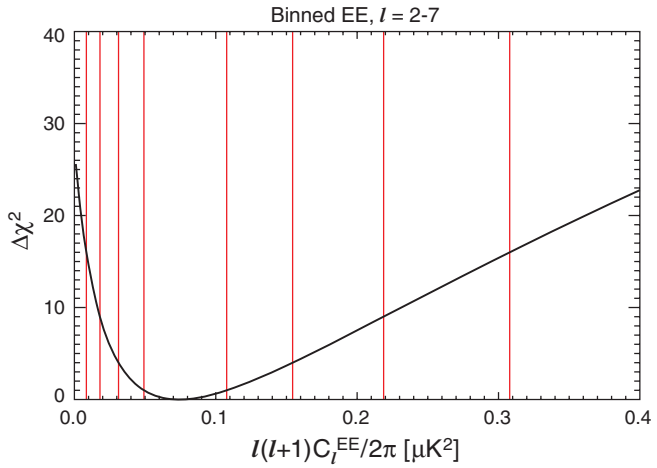

Figure 7. Relative χ^2 for a single bin of $l(l+1)C_l^{EE}/(2\pi)$ from $l = 2$–7, conditioned on the best-fit ΛCDM spectrum. For simplicity, we set $C_l^{TE} = 0$ for $l = 2$–7 for this evaluation, so that the constraint $C_l^{TE} \leqslant \sqrt{C_l^{TT} C_l^{EE}}$ will always be satisfied. The vertical red lines indicate where $\Delta\chi^2 = 1$, 4, 9, and 16, corresponding to 1σ, 2σ, 3σ, and 4σ confidence limits on EE. The EE=0 point in this bin has $\Delta\chi^2 = 26.5$; additionally, setting TE=0 in the 2–7 bin raises χ^2 by 3.5 relative to the best-fit ΛCDM TE spectrum. Thus, the full change in χ^2 between the best-fit model and the EE=TE=0 model is 30, corresponding to a 5.5σ detection of EE power in this bin, with $l(l+1)C_l^{EE}/(2\pi) = 0.074^{+0.034}_{-0.025}$ μK^2 (68% CL).

place an upper limit of

$$\mathcal{C}_{2-7}^{BB} \leqslant 0.055\ \mu\mathrm{K}^2\ (95\%\ \mathrm{CL}) \quad (8)$$

using the seven-year *WMAP* data, which is more than a factor of two lower than the five-year limit of $0.15\ \mu$K^2.

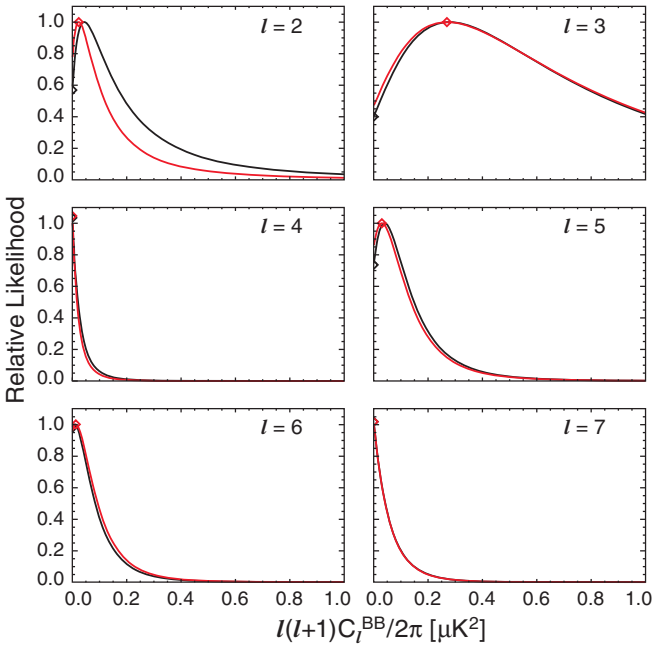

Figure 8. Conditional likelihoods of $l(l+1)C_l^{BB}/(2\pi)$ for $l = 2$–7 computed with the *WMAP* likelihood code. The Ka, Q, and V bands contribute to the low-l polarized pixel likelihood. In each panel, the black curve is the conditional likelihood for a given multipole when all other multipoles are held fixed at the value of the best-fit ΛCDM model (effectively zero, except for gravitational lensing) as indicated by the black diamonds. The red curve in each panel is the conditional likelihood when all other multipoles are held fixed at the maximum likelihood value of the spectrum, indicated by the red diamonds. The maximum likelihood spectrum was determined as stated in the caption to Figure 6.

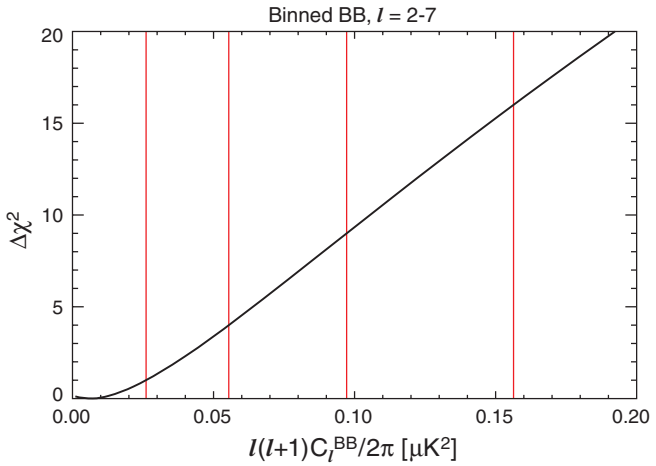

Figure 9. Relative χ^2 for a single bin of $l(l+1)C_l^{BB}/(2\pi)$ from $l = 2$–7, conditioned on the best-fit ΛCDM spectrum. The vertical red lines indicate where $\Delta\chi^2 = 1$, 4, 9, and 16, corresponding to 1σ, 2σ, 3σ, and 4σ confidence limits on BB. We find an upper limit of $l(l+1)C_l^{BB}/(2\pi) < 0.055$ μK^2 (95% CL).

The high-l EE spectrum is constructed using the polarized spectra that were used for the TE spectrum, discussed in Section 2.4. Figure 10 plots the seven-year *WMAP* data on top of the ΛCDM EE spectrum that best fits the *WMAP* data. Note that the high-l EE spectrum is not included in the likelihood code, so the theory curve is not a best fit to the high-l EE spectrum.

Using error bars with cosmic variance derived from the best-fit ΛCDM model, we find $\chi^2 = 830.6$, for the 777 degrees of freedom in the multipole range $24 \leqslant l \leqslant 800$. The probability to exceed this χ^2 value is 8.9%, which is low, but not significantly so. For a model with no EE spectrum, $\chi^2 = 897.3$. The

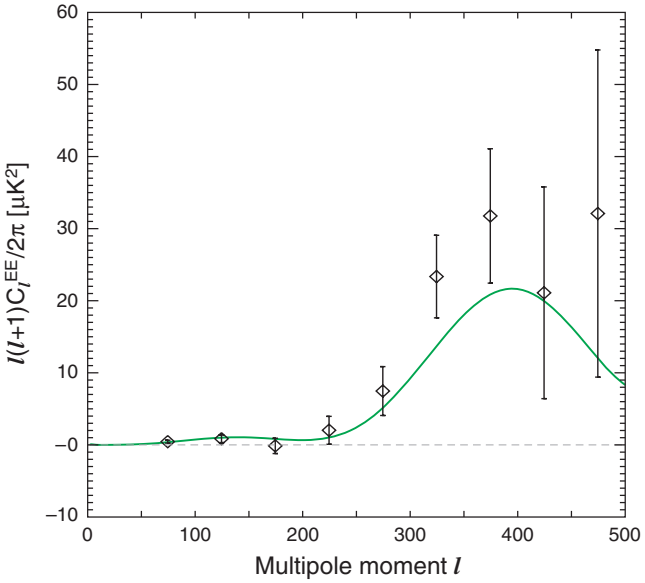

Figure 10. *WMAP* detects the high-l EE power spectrum. The green curve is the best-fit ΛCDM model power spectrum, and the data are a combination of Q-, V-, and W-band data. In the multipole range $24 \leqslant l \leqslant 800$, the detection is above 8σ.

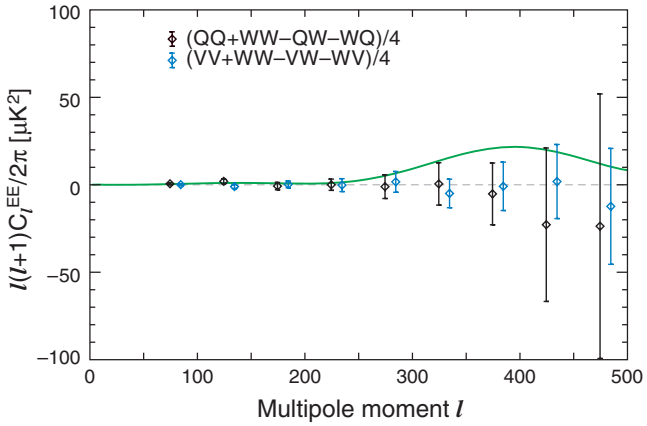

Figure 11. Q – W and V – W band difference spectra for EE are consistent with zero, as expected. The green line is the ΛCDM EE spectrum, which should not match this data, but is plotted to illustrate the size of the null-test error bars, compared to the detected signal.

difference is $\Delta\chi^2 = 66.7$, which is just over an 8σ detection of the high-l EE spectrum.

The data prefer an EE spectrum with higher amplitude than the best-fit ΛCDM model. To quantify this, we find the scale factor α that causes the theory EE spectrum to best fit the data, over the multipole range $24 \leqslant l \leqslant 800$. The scale factor is $\alpha = 1.52 \pm 0.21$. This indicates a 2.5σ preference for a higher amplitude EE spectrum, which we consider to be worth further investigation, but do not believe to be a significant deviation from the ΛCDM theory. Note that other experiments, such as QUaD (Brown et al. 2009), find the EE spectrum to be consistent with the prediction of the best-fit model.

To verify that we are not seeing the power spectrum in just one band and not the others, we take difference spectra among the Q, V, and W bands. Figure 11 shows two sets of difference spectra. These spectra are consistent with zero, as expected, and demonstrate that the EE power spectrum is present in all three frequency bands.

2.6. WMAP Likelihood Code

Before discussing cosmological parameter fits in the remainder of the paper, we review the *WMAP* likelihood code which forms the basis for the fits.

The basic structure of the likelihood code is unchanged from the five-year release. For the $l > 32$ temperature data, the model spectrum is compared to the MASTER spectrum, described above, using a Gaussian plus log-normal approximation to the likelihood, as described in Bond et al. (1998) and Verde et al. (2003). For $l \leqslant 32$, a Blackwell–Rao estimator is used to determine the likelihood of a model TT spectrum (Dunkley et al. 2009). This estimator encodes both the low-l spectrum and an accurate description of its non-Gaussian errors. It is constructed from a set of Gibbs samples that contain power spectra and CMB maps that are statistically consistent with the data (Wandelt et al. 2004; Jewell et al. 2004; Eriksen et al. 2004). The seven-year input to the Gibbs chain mimics the five-year input: we smooth the ILC map to 5° (Gaussian FWHM); degrade it to resolution $N_{\rm side} = 32$; and add Gaussian white noise with 2 μK rms to each pixel. The data are masked with the KQ85y7 mask degraded to $N_{\rm side} = 32$, and the Gibbs sampler is run to produce input for the Blackwell–Rao estimator; further details are given in Dunkley et al. (2009).

For the polarization data, we use a similar hybrid scheme: for the $l > 23$ TE data, we compare a model spectrum to the MASTER spectrum using a Gaussian likelihood. (TE is the only high-l polarization data used in the *WMAP* likelihood code.) For $l \leqslant 23$, the likelihood of model TE, EE, and BB spectra is obtained using a pixel-space likelihood which is based on the $N_{\rm side} = 8$ map mentioned in Section 2.4 and described in Page et al. (2007).

The likelihood code includes several important factors: mode coupling due to sky masking and non-uniform pixel weighting (due to non-uniform noise); beam window function uncertainty, which is correlated across the entire spectrum; and residual point source subtraction uncertainty, which is also highly correlated. The treatment of these effects is unchanged from the five-year analysis (Nolta et al. 2009; Dunkley et al. 2009).

Note added in revision—The results in this paper were prepared using version 4.0 of the *WMAP* likelihood. Since the initial submission of this paper, two small errors in the likelihood code came to light. (1) The original computation of the TT spectrum used an incorrect monopole subtraction which resulted in a small amount of excess power at high l and a corresponding elevation of the best-fit residual point source amplitude. Correcting the monopole subtraction reduced the high-l power slightly which produced a correspondingly lower residual point source amplitude, from 11.0×10^{-3} to 9.0×10^{-3} μK^2 sr. (2) Due to a simulation configuration error, the TE $f_{\rm sky}$ recalibration factor used in version 4.0 was 3.8% larger than the final value reported in Section 2.2.3. The first of these changes will not affect the simulations in Section 3, because they lack a monopole, and the new value for TE $f_{\rm sky}$ has been used for the Section 3 parameter recovery simulations. The goodness-of-fit statistics for the TT and TE spectra in Section 5 compare the best-fit ΛCDM theory spectrum from the version 4.0 Markov chains (with RECFAST version 1.4.2) to the version 4.1 likelihood data. See Appendix B for a comparison of parameters, when estimated with the original and updated versions of the code.

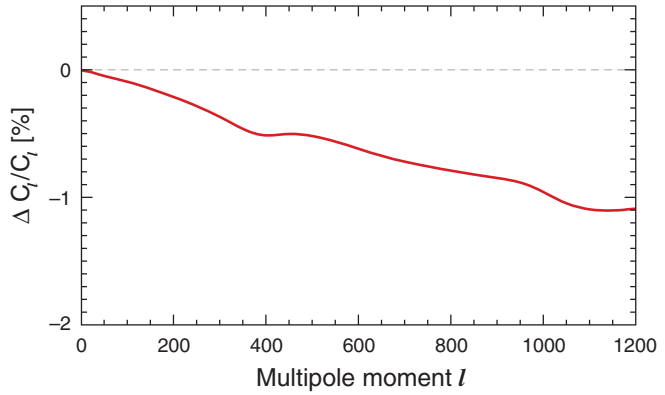

Figure 12. Red line in this figure represents the percentage change in the $C_l^{\rm TT}$ spectrum, due to the change in RECFAST from version 1.4.2 to version 1.5, including additional physics of the hydrogen atom.

2.6.1. CAMB

For computing theoretical power spectra, we use the Code for Anisotropies in the Microwave Background (CAMB; Lewis et al. 2000) which is based on the earlier code CMBFAST (Seljak & Zaldarriaga 1996).[16] Since 2008 the CAMB package has supported improved modeling of reionization, as follows. (1) inclusion of helium reionization, assuming that helium is singly reionized at the same time as hydrogen and doubly reionized at $z \sim 3.5$ (this slightly lowers the redshift of reionization for a given optical depth); (2) the width of reionization can be varied without changing the optical depth. We use a width $\Delta z = 0.5$ as standard. Seven-year reionization results are discussed in Section 4.2.7.

Shortly after the seven-year *WMAP* data were released, a new version of CAMB was made available, incorporating an updated version of the code used to model recombination: RECFAST (Seager et al. 1999, 2000; Wong et al. 2008; Scott & Moss 2009). The parameter recovery was run with RECFAST version 1.4.2, and the 2010 January version of CAMB updates this to RECFAST version 1.5. The primary change is in the optical depth, due to more accurate modeling of the physics of the hydrogen atom. Figure 12 shows how much the new version of RECFAST lowers the power spectrum, for a given set of cosmological parameters. The fractional lowering is largest at high l and is about 1% at $l = 1000$.

We discuss the effect of these changes in Appendix B. The parameter results presented in this paper and in Komatsu et al. (2011), use the original RECFAST version 1.4.2.

3. PARAMETER RECOVERY BIAS TESTS

In this section, we describe a test for bias in the *WMAP* parameter recovery process. The parameters of the basic ΛCDM model are the physical baryon density, $\Omega_b h^2$; the physical cold dark matter density, $\Omega_c h^2$; the dark energy density, in units of the critical density, Ω_Λ; the amplitude of primordial scalar curvature perturbations at $k = 0.002$ Mpc^{-1}, $\Delta^2_{\mathcal{R}}$; the power-law spectral index of primordial density (scalar) perturbations, n_s; and the reionization optical depth, τ. The above parameters are sampled with flat priors and are sufficiently constrained by the *WMAP* data that boundaries to these priors do not have to be specified. Nevertheless, our Markov chain code adds the following constraints: $0.001 < \Omega_b h^2 < 0.2, 0.0 < \Omega_c h^2 < 0.5$, $0 < \Omega_\Lambda$, $0.04 < h^2 < 1.0$, and $0.01 < \tau < 0.7$. In this model, the Hubble constant, $H_0 = 100h$ km s^{-1} Mpc^{-1}, is implicitly determined by the flatness constraint, $\Omega_b + \Omega_c + \Omega_\Lambda = 1$. The Sunyaev–Zel'dovich (SZ) effect is not included in these simulations, nor is the $A_{\rm SZ}$ parameter sampled; see Section 4.1 for details on this parameter. Table 1 gives a description of the parameters considered in this paper including both fundamental and derived quantities.

We generate 500 simulations of *WMAP* multi-frequency sky map data with known cosmological parameters, then verify that we recover the correct parameters from those data. To our knowledge, this is the first statistical test of the likelihood in which multiple independent realizations are combined to test for bias at the $\sim 0.1\sigma$ level. Since we start the test with simulated sky maps, this work tests: the MASTER deconvolution of the masked pseudo-power spectra; error propagation from maps to parameters; the code for combining V- and W-band data into a single TT spectrum; the code for combining Q-, V-, and W-band data into a single TE spectrum; the low-l pixel-space likelihood codes for temperature and polarization; and the algorithm for combining these hybrid inputs into a single likelihood per model.

There have been previous studies of the accuracy of the *WMAP* likelihood code. O'Dwyer et al. (2004) performed a Bayesian analysis of the one-year *WMAP* data and found temperature power spectra largely consistent with those reported by Hinshaw et al. (2003). However, they pointed out that the MASTER algorithm does not accurately represent the errors at low l. Chu et al. (2005) investigated cosmological parameters using the statistically exact Blackwell–Rao estimator as part of the likelihood code at low l and found shifts of up to 0.5σ, compared to the MASTER algorithm. These issues were addressed by Spergel et al. (2007) in the three-year *WMAP* analysis by using an $N_{\rm side} = 8$ pixel likelihood. Eriksen et al. (2007) pointed out that the $N_{\rm side} = 8$ code biased $C_l^{\rm TT}$ slightly high in the range $12 < l < 30$, which in turn biased n_s slightly low. As a result, the final version of Spergel et al. (2003) used an $N_{\rm side} = 16$ by code. Since then, the pixel likelihood code has been replaced with the Blackwell–Rao estimator, which accurately describes the $C_l^{\rm TT}$ power spectrum up to $l = 32$ (Dunkley et al. 2009).

The focus on n_s arises because simple inflation models predict its value to be slightly less than 1 (typically ~ 0.96, which is termed spectral "tilt") and the best-fit value from previous *WMAP* analyses is in that range. However, the uncertainty is such that the deviation from 1 is about 3σ, so small changes in the best-fit value can alter one's interpretation of significance. By comparing the *WMAP* likelihood code to a Gaussianized Blackwell–Rao estimator, Rudjord et al. (2009) report a bias in n_s of $+0.6\sigma$, which reduces the evidence for spectral tilt. In the results reported below, we do not find evidence for such a bias in the *WMAP* likelihood. In particular, using the seven-year *WMAP* data, we find $n_s = 0.963 \pm 0.014$ for a ΛCDM model fit.

The pipeline for the *WMAP* data has already been extensively tested by the *WMAP* team. This testing was in progress during the planning phase of the mission, and the pipeline continued to be refined after launch. Power spectrum reconstruction from maps was simulated for the first year data (Hinshaw et al. 2003). The likelihood code was calibrated (by adjusting the effective sky fraction, $f_{\rm sky,TT}$) with 100,000 simulations, so that the χ^2 values reported from the likelihood could be used for

[16] We use the 2008 November version of CAMB, which was updated to remove a bug affecting lensed non-flat models in 2009 February. The update was inadvertently not included in our current analysis, but we have checked that the effect on spectra is at the sub-percent level.

Table 1
Cosmological Parameter Definitions[a]

Parameter	Description
Fit parameters	
$\Omega_b h^2$	Physical baryon density
$\Omega_c h^2$	Physical cold dark matter density
Ω_Λ	Dark energy density ($w = -1$ unless otherwise noted—see below)
$\Delta^2_{\mathcal{R}}$	Amplitude of curvature perturbations, $k_0 = 0.002$ Mpc^{-1}
n_s	Spectral index of density perturbations, $k_0 = 0.002$ Mpc^{-1}
τ	Reionization optical depth
$A_{\rm SZ}$	Amplitude of the Sunyaev–Zel'dovich spectrum[b]
Derived parameters	
t_0	Age of the universe (Gyr)
H_0	Hubble parameter, $H_0 = 100h$ km s^{-1} Mpc^{-1}
σ_8	Amplitude of density fluctuations in linear theory, 8 h^{-1} Mpc scale
$z_{\rm eq}$	Redshift of matter-radiation equality
$z_{\rm reion}$	Redshift of reionization
Extended parameters	
$dn_s/d\ln k$	Running of scalar spectral index
r	Ratio of tensor to scalar perturbation amplitude, $k_0 = 0.002$ Mpc^{-1}
α_{-1}	Fraction of anti-correlated CDM isocurvature modes (see Section 4.2.3)
α_0	Fraction of uncorrelated CDM isocurvature modes (see Section 4.2.3)
Ω_k	Spatial curvature, $\Omega_k = 1 - \Omega_{\rm tot}$
w	Dark energy equation of state, $w = p_{\rm DE}/\rho_{\rm DE}$
$N_{\rm eff}$	Effective number of relativistic species (e.g., neutrinos)
$Y_{\rm He}$	Primordial helium fraction, by mass
Δ_z	Width of reionization (new parameter in CAMB, see Section 4.2.7)

Notes.
[a] Cosmological parameters discussed in this paper. A complete tabulation of the marginalized parameter values for each of the models discussed in this paper may be found at http://lambda.gsfc.nasa.gov
[b] The Sunyaev–Zel'dovich (SZ) amplitude is not sampled in the parameter recovery simulations, because the SZ effect is not included in the simulation power spectrum. $A_{\rm SZ}$ is sampled in the seven-year *WMAP* Markov chains, with a flat prior $0 < A_{\rm SZ} < 2$, but is unconstrained by the *WMAP* data. See Section 4.1.

goodness-of-fit tests as well as model comparison (Hinshaw et al. 2003; Verde et al. 2003). Simulations of multiple years of time ordered data have shown that maps can be reconstructed, the *WMAP* data calibrated from the annual dipole modulation, and correct maps of the microwave sky recovered.

Here, we present a statistical parameter extraction test: to check for bias in our likelihood code, we construct 500 realizations of multi-year, multi-frequency sky map data, then fit parameters from each realization independently. The input maps are transformed to power spectra and a likelihood code using the *WMAP* flight pipeline. The simulated inputs, which are also used in Section 5, are discussed in more detail in Appendix A.

To determine if the parameter fits are biased, one could sample parameters from a ΛCDM Markov chain for each realization individually, then form a weighted average. This would be fine if the recovered parameter likelihoods were Gaussian, but that is not guaranteed. The optimal way to combine the likelihoods is to multiply them, and then sample from the joint distribution. The product of these likelihoods would represent what we know about the universe if we had access to CMB data from 500 Hubble volumes. Perhaps the most obvious way to sample from this distribution is to run a Markov chain. However, each of the 500 likelihood functions involves an independent main program, set of data inputs, and running environment, so this solution is impractical.

Our approach is to use importance sampling. We want to draw samples from the joint distribution corresponding to the sum of $N = 500$ log likelihoods. Importance sampling draws samples from a covering distribution that is close to the desired distribution; it then weights the samples by the ratio of probability densities of the two distributions to correct for the difference between the two (Mackay 2003). This approach allows us to parallelize the processing as follows. We generate $M = 10{,}000$ samples from the covering distribution, compute the model spectra for each sample, and store them, then for each of N copies of the likelihood, we separately calculate the log likelihood for each sample spectrum. We add the log likelihoods, and subtract the log density of the Gaussian at that location, to form a weight for each sample. This set of weighted samples is effectively the joint likelihood of cosmological parameters over the 500 realizations. It is not necessary to load N copies of the likelihood code into memory, nor establish inter-process communication.

Determining a useful covering distribution is an iterative process. We start with a Gaussian model with no correlations between parameters, using only one realization, and gradually add realizations (shrinking the region of interest), updating the covariance matrix. In the end, we use a Gaussian distribution with a covariance matrix that is a factor of two larger than the covariance of the 500 combined likelihoods. This makes the width of the distribution $\sqrt{2}$ times "too large" in each dimension. Making the covariance matrix slightly larger than the desired distribution allows us to check for the possibility of large tails in the distribution of parameters. Because the Gaussian sampling distribution has tails which drop off exponentially quickly, it could (in principle) fail to properly sample the tail of a distribution which fell less rapidly. To test this possibility, an array of two-dimensional scatter plots is made with one cosmological parameter on each axis, and with the data points color-coded by weight. Visual inspection of these plots shows

Table 2
Parameter Recovery Bias Test[a]

Parameter[b]	Input Value[b]	Measured Bias[c]	Bias S/N[d]	Error Bar Accuracy[e]
$10^2\Omega_b h^2$	2.2622	0.0013 ± 0.0025	0.02	−0.035
$\Omega_c h^2$	0.11380	−0.00033 ± 0.00025	−0.06	0.074
Ω_Λ	0.72344	0.00167 ± 0.00128	0.06	0.039
$10^9\Delta^2_{\mathcal{R}}$	2.4588	−0.0160 ± 0.0050	−0.14	0.087
n_s	0.9616	0.0013 ± 0.0006	0.09	0.020
τ	0.08785	−0.00056 ± 0.00070	−0.04	0.042

Notes.
[a] Parameter recovery results based on 500 Monte Carlo simulations of seven-year *WMAP* data fit to the six-parameter ΛCDM model.
[b] Parameter and its input value in the 500 Monte Carlo realizations.
[c] Bias measured in the composite likelihood derived from 500 MC realizations, quoted as the mean and rms of the marginalized distribution. A positive number indicates that the recovered value was higher than the input value.
[d] Measured bias divided by rms of the marginalized likelihood derived from the *WMAP* data. The bias is less than 15% of the 1σ error the seven-year data.
[e] Fractional error in reported error bar. We compute the standard deviation of (output–input)/(output error), and then subtract 1. For the 150 realizations used (this column only), we expect fluctuations of ± 0.058 (1σ). Our results are compatible with this.

that the weights of the sampled distribution are largest in the center of the sampling distribution, so that the sampling distribution adequately covers the tails of the likelihood. To verify that we were not merely looking at the data in a misleading projection, we also perform a principal component analysis on the sampled points and redisplay them plotted on principal component axes. The weights remain highest in the center of the distribution.

The likelihood for these simulations differs from that used in the *WMAP* seven-year analysis in the following ways. Most of these differences are for computational convenience. Because of disk space and computational time limitations, we do not simulate 500 sets of the time ordered data and map reconstruction; we begin with the maps. No foregrounds are included, for simplicity. No beam error is included, so we do not have to simulate small differences in deconvolution. No unresolved point source error is included, and we do not introduce point sources into the maps. CAMB is run at slightly higher accuracy, but this has a negligible effect on parameters. The $N_{\rm side} = 16$ pixel likelihood is used for $l \leqslant 30$ temperature, instead of the Gibbs likelihood, because while the Gibbs likelihood runs more rapidly, the pixel likelihood data products are much faster to generate. The SZ effect is not included in the input spectrum, and so we do not attempt to fit it (unlike the seven-year Markov chain analysis, discussed in Section 4.1). While these differences mean that the parameter recovery simulations do not simulate every part of the data analysis, they simulate a substantial portion.

Since we have 500 times more data in these parameter recovery simulations than in the seven-year *WMAP* data, a level of bias well below 1σ is detectable in the simulations, whereas it is not in the *WMAP* flight data. The samples from the importance sampling can be fit with a six-dimensional Gaussian. Using this Gaussian to approximate the joint likelihood of all 500 realizations, the input parameters have $\chi^2 = 27$ for 6 degrees of freedom, which indicates a strong detection of a difference between the input and recovered parameters. The assumption of Gaussianity is reasonably good here, but the detection can also be stated without that assumption. Suppose one draws a line (in this six-dimensional parameter space) between the input parameters and the mean of the recovered parameters and then projects all the sampled points onto that line. Then, one can determine how far away the input parameters are from the recovered parameters by calculating how much weight is on either side of the line from the input parameters. In this case, all of the weight except for one point is on one side of the line. Because that one point is out in the tail of the distribution, it has a weight well below average, and much less than one part in 10,000 of the weight is on the far side of the input parameters. This indicates that the input parameters are not consistent with the likelihood of recovered parameters. Both of these arguments indicate that the input parameters are biased.

However, this analysis shows that the recovered parameters have very little bias compared to their uncertainties. The measured level is less than 15% of the seven-year error on each parameter, and complete results are given in Table 2. Since the magnitude of the bias is small compared to the errors in the seven-year *WMAP* data, and since it will be different for different cosmological models, we do not attempt to remove it from the recovered parameters.

Table 2 shows that we tend to overestimate n_s by 0.09σ. Using a different likelihood code on the five-year data, Rudjord et al. (2009) found a value of n_s that was 0.6σ higher than our five-year result, but with the same predicted uncertainty. Since we have demonstrated that our likelihood is not biased at this level, we must either conclude that (1) there is some bias in the Rudjord et al. form of the likelihood, (2) there is some undetected residual bias in our likelihood, or (3) that both are (practically) unbiased and that different likelihood approximations can lead to parameter estimates that differ by this magnitude. To resolve this question, one should evaluate both likelihood functions on common data simulations, then jointly study the performance of the derived parameter ensembles. Our parameter recovery simulations show that the *WMAP* likelihood produces only a small bias when averaged over many CMB realizations. This does not imply that it is a better approximation to the exact likelihood than, e.g., the Rudjord et al. form, thus a joint comparison over many data realizations would be useful. To get a very rough sense of how large a difference one might expect, in case (3), above, we consider a toy model in which we estimate the variance of N random numbers from two partially overlapping subsets of the N numbers. In a case where 10% of the total data sample is disjoint (i.e., 5% in each subsample is independent) the two estimates of the parent

variance differ, statistically, by 0.3σ, where σ is the rms of each of the subsample estimates. Thus, for two likelihood functions to produce parameter estimates that differ by 0.6σ (at 95% confidence), the two functions must, in effect, be re-weighting 5% of the data. Given the similar construction of the two likelihood functions, this seems unlikely, so further study will be required to understand this difference.

We can also use the parameter recovery simulations to verify that our error estimates are correct. For each of 150 of the data realizations, we use a Markov chain to compute the mean and 68% confidence interval for each parameter. We then examine the distribution of the quantity (output value–input value)/(output error) which should have a unit variance. The results are shown in the last column of Table 2, where we find that the errors predicted by the Markov Chain agree with the true errors, to within the noise expected from the limited number of realizations.

4. COSMOLOGICAL PARAMETERS FROM *WMAP*

In this section, we discuss the determination of cosmological parameters using only the seven-year *WMAP* data. The measurements obtained by combining seven-year *WMAP* data with other cosmological data sets are presented in Komatsu et al. (2011). Our analysis employs the same Monte Carlo Markov Chain (MCMC) formalism used in previous analyses (Spergel et al. 2003, 2007; Verde et al. 2003; Dunkley et al. 2009; Komatsu et al. 2009). The MCMC formalism naturally produces parameter likelihoods that are marginalized over all other fit parameters in the model. Throughout this paper, we quote best-fit values as the mean of the marginalized likelihood, unless otherwise stated (e.g., upper limits). Lower and upper error limits correspond to the 16% and 84% points in the marginalized cumulative distribution, unless otherwise stated.

4.1. Six-parameter ΛCDM

The ΛCDM parameters used are the same as in Section 3, and mentioned in Table 1, except that $A_{\rm SZ}$ is now also sampled. This is a scale factor for the predicted Sunyaev–Zel'dovich spectrum (Komatsu & Seljak 2002), measured at *V* band, which we add to the TT power spectrum as in Spergel et al. (2007). In the Markov chains, this parameter is given a flat prior $0 < A_{\rm SZ} < 2$, but is unconstrained by the *WMAP* data, so its posterior distribution is very flat over this region. Failing to include the SZ effect does not significantly raise the χ^2 of the fit, so only six parameters are needed to provide a good fit to the *WMAP* power spectra, and we sample $A_{\rm SZ}$ only to marginalize over it.

The ΛCDM parameters best fit to the seven-year *WMAP* data are given in Table 3, which also lists values derived from the five-year data for comparison. The results are consistent, with the seven-year measurements giving smaller uncertainties, as expected. The parameters that show the greatest improvement are those that most depend on the amplitude of the third acoustic peak and the low-*l* EE polarization: $\Omega_b h^2$, $\Omega_c h^2$, and τ, all of which are measured about 12% more precisely. The derived late-time matter fluctuation amplitude, σ_8 (which depends on $\Omega_c h^2$ and τ), is measured 17% more precisely by the new data. In Section 4.3, we consider the overall change in allowable parameter-space volume offered by the seven-year data.

As discussed in Section 5, this basic ΛCDM model continues to fit the seven-year *WMAP* data quite well. Indeed, none of the additional parameters considered below provide a statistically better fit to the seven-year *WMAP* data, after accounting for the fewer degrees of freedom in the fits.

Table 3
Six-parameter ΛCDM Fit[a]

Parameter	Seven-year Fit	Five-year Fit
Fit parameters		
$10^2\Omega_b h^2$	$2.258^{+0.057}_{-0.056}$	2.273 ± 0.062
$\Omega_c h^2$	0.1109 ± 0.0056	0.1099 ± 0.0062
Ω_Λ	0.734 ± 0.029	0.742 ± 0.030
$\Delta^2_{\mathcal{R}}$	$(2.43 \pm 0.11) \times 10^{-9}$	$(2.41 \pm 0.11) \times 10^{-9}$
n_s	0.963 ± 0.014	$0.963^{+0.014}_{-0.015}$
τ	0.088 ± 0.015	0.087 ± 0.017
Derived parameters		
t_0	13.75 ± 0.13 Gyr	13.69 ± 0.13 Gyr
H_0	71.0 ± 2.5 km s^{-1} Mpc^{-1}	$71.9^{+2.6}_{-2.7}$ km s^{-1} Mpc^{-1}
σ_8	0.801 ± 0.030	0.796 ± 0.036
Ω_b	0.0449 ± 0.0028	0.0441 ± 0.0030
Ω_c	0.222 ± 0.026	0.214 ± 0.027
$z_{\rm eq}$	3196^{+134}_{-133}	3176^{+151}_{-150}
$z_{\rm reion}$	10.5 ± 1.2	11.0 ± 1.4

Note. [a] Models fit to *WMAP* data only. See Komatsu et al. (2011) for additional constraints.

4.2. Extended Cosmological Models

In this section, we examine the constraints that can be placed on augmented ΛCDM models (and one non-Λ model). In the first group, we consider parameters that introduce "new physics": tensor modes, a running spectral index, isocurvature modes, spatial curvature, and non-Λ dark energy. In the second group, we relax the constraints on "standard physics" by allowing the effective neutrino number and the primordial helium abundance to vary. We also allow the reionization profile to vary.

4.2.1. Gravitational Waves

The amplitude of tensor modes, or gravitational waves, in the early universe may be written as

$$\Delta^2_h(k) \equiv \frac{k^3 P_h(k)}{2\pi^2}, \tag{9}$$

where $P_h(k)$ is the power spectrum of tensor perturbations at wave number k and the normalization of $P_h(k)$ is as given by Komatsu et al. (2009). This form is comparable to the curvature perturbation amplitude,

$$\Delta^2_{\mathcal{R}}(k) \equiv \frac{k^3 P_{\mathcal{R}}(k)}{2\pi^2}. \tag{10}$$

The dimensionless tensor-to-scalar ratio is defined as

$$r \equiv \frac{\Delta^2_h(k)}{\Delta^2_{\mathcal{R}}(k)} \tag{11}$$

evaluated at $k = 0.002$ Mpc^{-1}. In the Markov chain, we set a flat prior on r, and require $r > 0$.

We do not detect gravitational waves from inflation with the seven-year *WMAP* data, however the upper limits are 16% lower: $r < 0.36$ (95% CL) compared to $r < 0.43$ (95% CL). Figure 13 shows the two-dimensional likelihood contours for r versus the other ΛCDM parameters using both the five-year and seven-year *WMAP* data. This shows both the improved upper limit on r and the correlations with the other measured parameters, especially

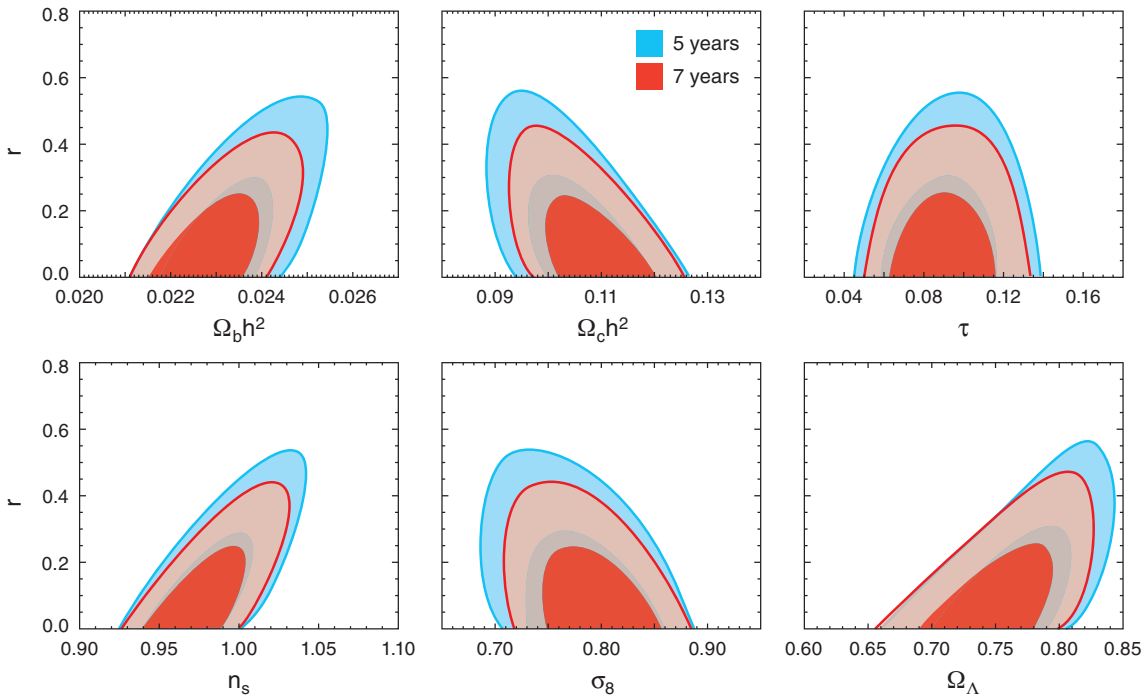

Figure 13. Gravitational wave constraints from the seven-year *WMAP* data, expressed in terms of the tensor-to-scalar ratio, r. The red contours show the 68% and 95% confidence regions for r compared to each of the six ΛCDM parameters using the seven-year data. The blue contours are the corresponding five-year results. We do not detect gravitational waves with the new data; when we marginalize over the six ΛCDM parameters the seven-year limit is $r < 0.36$ (95% CL), compared to the five-year limit of $r < 0.43$ (95% CL). Tighter limits apply when *WMAP* data are combined with H_0 and BAO constraints (Komatsu et al. 2011).

the matter densities and n_s. The limits quoted above arise from all of the power spectra measured by *WMAP* with the greatest power coming from the shape of the TT spectrum. Komatsu et al. (2011) consider the constraints that arise from polarization alone and show that the limits improve from $r < 1.6$ to $r < 0.93$ using the five-year and seven-year data, respectively.

4.2.2. Scale-dependent Spectral Index

Some inflation models predict a scale dependence or "running" in the (nearly) power-law spectrum of scalar perturbations. This is conveniently parameterized by the logarithmic derivative of the spectral index, $dn_s/d\ln k$, which gives rise to a spectrum of the form (Kosowsky & Turner 1995)

$$\Delta^2_{\mathcal{R}}(k) = \Delta^2_{\mathcal{R}}(k_0)\left(\frac{k}{k_0}\right)^{n_s(k_0)-1+\frac{1}{2}\ln(k/k_0)dn_s/d\ln k}, \quad (12)$$

with $k_0 = 0.002$ Mpc^{-1}. In the Markov chain, we use a flat prior on $dn_s/d\ln k$.

We do not detect a statistically significant (i.e., >95% CL) deviation from a pure power-law spectrum with the seven-year *WMAP* data. The allowed range of $dn_s/d\ln k$ is both closer to zero and has a smaller confidence range using the seven-year data: $dn_s/d\ln k = -0.034 \pm 0.026$ compared to $dn_s/d\ln k = -0.037 \pm 0.028$ from the five-year data.

If we allow *both* tensors and running as additional primordial degrees of freedom, the data prefer a slight negative running, but still at less than 2σ. The joint constraint on all parameters in this model is significantly tighter with the seven-year data (see Section 4.3). The seven-year constraints on models with additional power spectrum degrees of freedom are given in Table 4.

4.2.3. Isocurvature Modes

In addition to adiabatic fluctuations, where different species fluctuate in phase to produce curvature fluctuations, it is possible to have an overdensity in one species compensate for an underdensity in another without producing a curvature. These entropy, or isocurvature perturbations have a measurable effect on the CMB by shifting the acoustic peaks in the power spectrum. For cold dark matter and photons, we define the field

$$\mathcal{S}_{c,\gamma} \equiv \frac{\delta\rho_c}{\rho_c} - \frac{3\delta\rho_\gamma}{4\rho_\gamma} \quad (13)$$

(Bean et al. 2006; Komatsu et al. 2009). The relative amplitude of its power spectrum is parameterized by α,

$$\frac{\alpha}{1-\alpha} \equiv \frac{P_{\mathcal{S}}(k_0)}{P_{\mathcal{R}}(k_0)}, \quad (14)$$

with $k_0 = 0.002$ Mpc^{-1}.

We consider two types of isocurvature modes: those which are completely uncorrelated with the curvature modes (with amplitude α_0), motivated with the axion model, and those which are anti-correlated with the curvature modes (with amplitude α_{-1}), motivated with the curvaton model. For the latter, we adopt the convention in which anti-correlation increases the power at low multipoles (Komatsu et al. 2009). For both α_0 and α_{-1}, we adopt a flat prior and require $\alpha_0 > 0$, $\alpha_{-1} > 0$.

The constraints on both types of isocurvature modes are given in Table 5. We do not detect a significant contribution from either type of perturbation in the seven-year data. The limit on uncorrelated modes improves the most with the new data: from $\alpha_0 < 0.16$ (95% CL) to $\alpha_0 < 0.13$ (95% CL) using the five-year and seven-year data, respectively. Table 5 also shows that the standard ΛCDM parameters are only weakly affected by the

Table 4
Primordial Power Spectrum Constraints[a]

Parameter	ΛCDM+Tensors	ΛCDM+Running	ΛCDM+Tensors+Running
Fit parameters			
$\Omega_b h^2$	$0.02313^{+0.00073}_{-0.00072}$	$0.02185^{+0.00082}_{-0.00081}$	$0.02221^{+0.00085}_{-0.00089}$
$\Omega_c h^2$	$0.1068^{+0.0062}_{-0.0063}$	$0.1182^{+0.0084}_{-0.0085}$	$0.1157^{+0.0086}_{-0.0085}$
Ω_Λ	0.757 ± 0.031	$0.688^{+0.052}_{-0.051}$	$0.707^{+0.049}_{-0.050}$
$\Delta^2_{\mathcal{R}}$	$(2.28 \pm 0.15) \times 10^{-9}$	$(2.42 \pm 0.11) \times 10^{-9}$	$(2.23^{+0.17}_{-0.18}) \times 10^{-9}$
n_s	$0.982^{+0.020}_{-0.019}$	$1.027^{+0.050}_{-0.051}$	1.076 ± 0.065
τ	0.091 ± 0.015	0.092 ± 0.015	0.096 ± 0.016
r	< 0.36 (95% CL)	...	< 0.49 (95% CL)
$dn_s/d\ln k$	...	-0.034 ± 0.026	-0.048 ± 0.029
Derived parameters			
t_0	13.63 ± 0.16 Gyr	$13.87^{+0.17}_{-0.16}$ Gyr	13.79 ± 0.18 Gyr
H_0	73.5 ± 3.2 km s^{-1} Mpc^{-1}	67.5 ± 3.8 km s^{-1} Mpc^{-1}	$69.1^{+4.0}_{-4.1}$ km s^{-1} Mpc^{-1}
σ_8	0.787 ± 0.033	0.818 ± 0.033	0.808 ± 0.035

Notes. [a] Models fit to seven-year *WMAP* data only. See Komatsu et al. (2011) for additional constraints.

Table 5
Constraints on Isocurvature Modes[a]

Parameter	ΛCDM[b]	ΛCDM+Anti-correlated[c]	ΛCDM+Uncorrelated[d]
Fit parameters			
$\Omega_b h^2$	$0.02258^{+0.00057}_{-0.00056}$	$0.02293^{+0.00060}_{-0.00061}$	$0.02315^{+0.00071}_{-0.00072}$
$\Omega_c h^2$	0.1109 ± 0.0056	$0.1058^{+0.0057}_{-0.0058}$	$0.1069^{+0.0059}_{-0.0060}$
Ω_Λ	0.734 ± 0.029	0.766 ± 0.028	0.758 ± 0.030
$\Delta^2_{\mathcal{R}}$	$(2.43 \pm 0.11) \times 10^{-9}$	$(2.24 \pm 0.13) \times 10^{-9}$	$(2.38 \pm 0.11) \times 10^{-9}$
n_s	0.963 ± 0.014	0.984 ± 0.017	0.982 ± 0.020
τ	0.088 ± 0.015	0.088 ± 0.015	0.089 ± 0.015
α_{-1}	...	< 0.011 (95% CL)	...
α_0	...	...	< 0.13 (95% CL)
Derived parameters			
t_0	13.75 ± 0.13 Gyr	13.58 ± 0.15 Gyr	13.62 ± 0.16 Gyr
H_0	71.0 ± 2.5 km s^{-1} Mpc^{-1}	$74.5^{+3.1}_{-3.0}$ km s^{-1} Mpc^{-1}	73.6 ± 3.2 km s^{-1} Mpc^{-1}
σ_8	0.801 ± 0.030	$0.784^{+0.033}_{-0.032}$	0.785 ± 0.032

Notes.
[a] Models fit to seven-year *WMAP* data only. See Komatsu et al. (2011) for additional constraints.
[b] Repeated from Table 3 for comparison.
[c] Adds curvaton-type isocurvature perturbations (Komatsu et al. 2011).
[d] Adds axion-type isocurvature perturbations (Komatsu et al. 2011).

isocurvature degrees of freedom. Komatsu et al. (2011) derive analogous constraints using a combination of *WMAP* plus other data. They find limits that are roughly a factor of two lower than the *WMAP*-only limits.

4.2.4. Spatial Curvature

The basic ΛCDM model of the universe is flat, with $\Omega_k = 1 - \Omega_{\rm tot} = 0$. There is a compelling theoretical case for a flat universe in general relativity, arising from the apparent paradox that a flat geometry is dynamically unstable. That is, in order for the curvature to be acceptably small today, say $|\Omega_k| < 1$, the curvature in the early universe had to be extraordinarily fine tuned. Cosmological inflation achieves this by expanding the primordial curvature scale, if any, to super-horizon scales today.

With knowledge of the redshift of matter-radiation equality, the acoustic scale can be accurately computed for use as a standard ruler at the epoch of recombination. The first acoustic peak in the CMB then provides a means to measure the angular diameter of the acoustic scale at the surface of last scattering. If we have independent knowledge of the local distance–redshift relation (the Hubble constant, H_0) we can infer the physical distance to the last scattering surface, and hence the geometry of the universe. If we assume nothing about H_0 we are left with a geometric degeneracy which is illustrated in Figure 14.

Assuming ΛCDM dynamics, *WMAP* data alone provide a remarkably simple constraint on the geometry and matter-energy content in the universe. The geometric degeneracy in the seven-year data is well described by $\Omega_k = -0.2654 + 0.3697\Omega_\Lambda$ (the dashed line in Figure 14). We have placed a flat prior on Ω_k, and we now also constrain $\Omega_\Lambda > 0$. The figure also quantitatively illustrates how knowledge of the Hubble constant fixes the geometry, $\Omega_\Lambda + \Omega_m$, and vice versa. The points in the plot are culled from the Markov Chain that samples this model and their color is coded by the value of the Hubble constant for that sample. As one moves down the degeneracy line, the Hubble constant must decrease for the model to remain consistent with the geometry imposed by the CMB. For a *flat* universe, the seven-year data give $H_0 = 71.0 \pm 2.5$ km s^{-1} Mpc^{-1} (Table 3), in excellent agreement with more traditional measurements of the Hubble constant, e.g., Riess et al. (2009).

If we allow curvature as a parameter, the seven-year *WMAP* data improve on the five-year constraint by 11% to

Table 6
Constraints on Curvature and Dark Energy[a]

Parameter	ΛCDM[b]	OΛCDM[c]	wCDM[d]
Fit parameters			
$\Omega_b h^2$	$0.02258^{+0.00057}_{-0.00056}$	$0.02229^{+0.00058}_{-0.00057}$	$0.02258^{+0.00063}_{-0.00062}$
$\Omega_c h^2$	0.1109 ± 0.0056	$0.1117^{+0.0053}_{-0.0055}$	0.1112 ± 0.0058
Ω_Λ	0.734 ± 0.029	< 0.77 (95% CL)	$0.741^{+0.095}_{-0.099}$
$\Delta^2_{\mathcal{R}}$	$(2.43 \pm 0.11) \times 10^{-9}$	$(2.48 \pm 0.11) \times 10^{-9}$	$(2.43 \pm 0.12) \times 10^{-9}$
n_s	0.963 ± 0.014	0.955 ± 0.014	0.964 ± 0.015
τ	0.088 ± 0.015	0.086 ± 0.015	$0.088^{+0.016}_{-0.015}$
Ω_k	...	$-0.080^{+0.071}_{-0.093}$	...
w	...	...	$-1.12^{+0.42}_{-0.43}$
Derived parameters			
t_0	13.75 ± 0.13 Gyr	$15.9^{+2.0}_{-1.7}$ Gyr	$13.75^{+0.29}_{-0.27}$ Gyr
H_0	71.0 ± 2.5 km s^{-1} Mpc^{-1}	53^{+13}_{-15} km s^{-1} Mpc^{-1}	75^{+15}_{-14} km s^{-1} Mpc^{-1}
σ_8	0.801 ± 0.030	$0.762^{+0.044}_{-0.047}$	0.83 ± 0.14

Notes.
[a] Models fit to seven-year *WMAP* data only. See Komatsu et al. (2011) for additional constraints.
[b] Repeated from Table 3 for comparison.
[c] Adds spatial curvature as a parameter, with $w \equiv -1$. $\Omega_\Lambda > 0$ is imposed as a prior.
[d] Adds dark energy equation of state as a parameter, with $\Omega_k \equiv 0$. $w > -2.5$ is imposed as a prior.

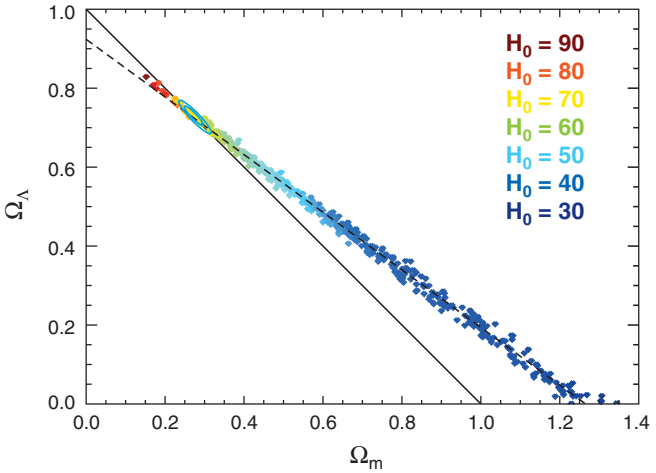

Figure 14. Range of non-flat models consistent with the *WMAP* seven-year data. The plotted points are drawn from the Markov chain (ΛCDM, with curvature, fit to *WMAP* data only); the color of each point indicates the Hubble constant for that element in the chain, as indicated in the legend. Due to the geometric degeneracy, CMB data alone do not strongly constrain closed models with $\Omega_\Lambda + \Omega_m > 1$, provided a low Hubble constant is tolerated, see Table 6. The dashed line parameterizes the geometric degeneracy in the seven-year data: $\Omega_k = -0.2654 + 0.3697\Omega_\Lambda$. When *WMAP* data are combined with H_0 and BAO data, the result strongly favors a flat universe: $0.99 < \Omega_{\rm tot} < 1.01$ (95% CL) (Komatsu et al. 2011). The joint constraints, shown as 68% and 95% blue contours, provide compelling support for basic ΛCDM.

$\Omega_k = -0.080^{+0.071}_{-0.093}$. While this result is consistent with a flat universe, the preferred model is slightly closed and has a relatively low Hubble constant due to the geometric degeneracy, $H_0 = 53^{+13}_{-15}$ km s^{-1} Mpc^{-1}. Therefore, if we impose local distance scale measurements in the form of H_0 and BAO data, the limits on curvature tighten significantly to $\Omega_k = -0.0023^{+0.0054}_{-0.0056}$ (Komatsu et al. 2011).

4.2.5. Non-Λ Dark Energy

Dark energy is believed to be driving the present-day acceleration of the universe. Current measurements are consistent with the dark energy being a cosmological constant or vacuum energy. If it is not a cosmological constant, then its physical density may change with the expansion of the universe. This, in turn, would affect the expansion history and the rate of large-scale structure growth in the universe. The evolution of its physical density is governed by its equation of state $w = p/\rho$ where p is the pressure of the dark energy and ρ its density. The cosmological constant has an equation of state $w = -1$. It would be tremendously important if observations could determine that $w \neq -1$ since that would rule out the prime candidate for the dark energy and provide important new clues about physics.

Since the CMB primarily probes the high redshift universe ($z \sim 1000$), and the effects of dark energy only start to dominate at relatively low redshift ($z \sim 2$), the CMB is not especially sensitive to subtle properties of the dark energy. Nonetheless, meaningful constraints on the equation of state can be inferred from the seven-year *WMAP* data. If we assume that the universe is flat but let w be a parameter in the Friedmann equation (with a flat prior on w, $-2.5 < w < 0$, and $w' = 0$), we obtain the constraints given in Table 6. In particular, the seven-year data give $w = -1.12^{+0.42}_{-0.43}$, which is consistent with a cosmological constant. Komatsu et al. (2011) investigate the constraints imposed when seven-year *WMAP* data are combined with other observations. With BAO and Hubble constant measurements added, they find $w = -1.10 \pm 0.14$, which provides compelling limits on w *without* using Type Ia supernovae (SNe) data. When SNe data are included, the result becomes $w = -0.980 \pm 0.053$, but the quoted error does not include systematic errors in the SNe, which are comparable to the statistical errors. Accounting for this would produce a final uncertainty that is roughly half the size of the error without SNe data.

If we relax the assumption that $w' = 0$ and/or $\Omega_k = 0$, the constraints on w weaken (Komatsu et al. 2011). This points to the need for more accurate and precise measurements of the expansion history and growth rate of structure if we are to gain further clues about dark energy from cosmology.

4.2.6. Neutrinos

Neutrinos affect the CMB spectrum in a variety of ways; one is by providing relativistic degrees of freedom to the plasma prior

Table 7
Constraints on Neutrino Properties[a]

Parameter	ΛCDM[b]	ΛCDM+$N_{\rm eff}$[c]	ΛCDM+$\sum m_\nu$[d]
Fit parameters			
$\Omega_b h^2$	$0.02258^{+0.00057}_{-0.00056}$	$0.02260^{+0.00055}_{-0.00054}$	$0.02219^{+0.00061}_{-0.00062}$
$\Omega_c h^2$	0.1109 ± 0.0056	$0.162^{+0.041}_{-0.038}$	0.1122 ± 0.0055
Ω_Λ	0.734 ± 0.029	$0.731^{+0.029}_{-0.030}$	$0.660^{+0.062}_{-0.063}$
$\Delta^2_{\mathcal{R}}$	$(2.43 \pm 0.11) \times 10^{-9}$	$(2.39 \pm 0.11) \times 10^{-9}$	$(2.50 \pm 0.13) \times 10^{-9}$
n_s	0.963 ± 0.014	$0.992^{+0.022}_{-0.023}$	0.953 ± 0.017
τ	0.088 ± 0.015	$0.088^{+0.014}_{-0.015}$	0.086 ± 0.014
$N_{\rm eff}$	...	> 2.7 (95% CL)	...
$\sum m_\nu$	...	...	< 1.3 eV (95% CL)
Derived parameters			
t_0	13.75 ± 0.13 Gyr	$11.9^{+1.2}_{-1.3}$ Gyr	$14.09^{+0.25}_{-0.26}$ Gyr
H_0	71.0 ± 2.5 km s^{-1} Mpc^{-1}	$82.6^{+8.9}_{-8.7}$ km s^{-1} Mpc^{-1}	$65.0^{+4.4}_{-4.5}$ km s^{-1} Mpc^{-1}
σ_8	0.801 ± 0.030	0.903 ± 0.077	$0.685^{+0.079}_{-0.078}$

Notes.
[a] Models fit to seven-year *WMAP* data only. See Komatsu et al. (2011) for additional constraints.
[b] Repeated from Table 3 for comparison.
[c] Allows effective number of relativistic species to vary (cf. $N_{\rm eff}$=3.04). $N_{\rm eff} < 10$ is imposed as a prior.
[d] Adds neutrino mass, $\sum m_\nu$, as a parameter, assuming $N_{\rm eff}$=3.04 and degenerate mass eigenstates.

to recombination. Since neutrinos, or other relativistic species, are not coupled to the photon-baryon fluid, they free-stream out of overdensities and damp the acoustic oscillations prior to recombination. This action suppresses the peaks in the angular power spectrum somewhat; the amplitude of the effect depends on the effective number of relativistic degrees of freedom. Using the seven-year *WMAP* data we place a 95% CL lower limit of $N_{\rm eff} > 2.7$ (95% CL) on the number of relativistic degrees of freedom, for a flat prior $0 < N_{\rm eff} < 10$. (The standard model has $N_{\rm eff} = 3.04$.) This new limit is 17% higher than the five-year limit of $N_{\rm eff} > 2.3$ (95% CL)—due to the improved third peak measurement—and is now quite close to the standard model value.

The mean energy of a relativistic neutrino at the epoch of recombination is $\langle E \rangle = 0.58$ eV. In order for the CMB power spectrum to be sensitive to a non-zero neutrino mass, at least one species of neutrino must have a mass in excess of this mean energy (Komatsu et al. 2009). If one assumes that there are $N_{\rm eff} = 3.04$ neutrino species with degenerate mass eigenstates, this would suggest that the lowest total mass that could be detected with CMB data is $\sum m_\nu \sim 1.8$ eV. Using a refined argument, Ichikawa et al. (2005) argue that one could reach ~1.5 eV. When we add $\sum m_\nu$ as a parameter to the ΛCDM model (and a flat prior on the physical neutrino density, $\Omega_\nu h^2$, constrained by $\Omega_\nu h^2 > 0$), we obtain the fit given in Table 7, specifically $\sum m_\nu < 1.3$ eV (95% CL), which is unchanged from the five-year result and is slightly below the basic limits just presented. Note that these results come from the *WMAP* data alone. Tighter limits may be obtained by combining CMB data with measurements of structure formation, as discussed in Komatsu et al. (2011) and references therein.

4.2.7. Width of Reionization

Effective with the 2008 March version of the code CAMB (Lewis 2008), a new parameter has been added which allows users to vary the reionization profile while holding the total optical depth fixed. The basic profile is a smooth ramp in redshift space and the parameter, Δ_z, changes the slope of the ramp about its midpoint in such a way as to preserve the total optical depth.

We have added Δ_z as a parameter to the basic ΛCDM model, with a flat prior in the range $0.5 < \Delta_z < 15$, and present the results in Table 8.

4.2.8. Primordial Helium Abundance

Helium is thought to be synthesized in the early universe via BBN. Given the *WMAP* measurement of the baryon-to-photon ratio, η, the BBN-predicted yield for helium is $Y_{\rm He} = 0.249$ (Steigman 2007). To date, the best technique for measuring the primordial abundance has been to observe stars in H II regions: in these systems, the helium abundance as a function of metallicity can be observed and the relation can be regressed to zero metallicity, which is presumed to give the primordial abundance (Gruenwald et al. 2002; Izotov & Thuan 2004; Olive & Skillman 2004; Fukugita & Kawasaki 2006; Peimbert et al. 2007) as reviewed by Steigman (2007).

Primordial helium affects the time profile of recombination which, in turn, affects the CMB angular power spectrum, especially the third acoustic peak. With *WMAP*'s improved measurement of this peak, it is now possible to let $Y_{\rm He}$ be a fitted parameter in the ΛCDM model. We use a flat prior with $0.01 < Y_{\rm He} < 0.8$. We present the results of this fit in Table 8 and call out the helium abundance specifically: $Y_{\rm He} = 0.28^{+0.14}_{-0.15}$. This result is consistent with the BBN prediction and suggests the existence of pre-stellar helium, at the $\sim 2\sigma$ level. Komatsu et al. (2011) consider the constraints that can be applied when higher-resolution CMB data are included in the fit. They find that the combined CMB data produce, for the first time, evidence for pre-stellar helium at $> 3\sigma$.

4.3. Volume Change

The tables presented in this section quote parameter uncertainties for marginalized one-dimensional likelihood profiles. With the seven-year and five-year results side by side, one could infer the improvement in precision for any given parameter in any given model fit, and we have called out examples in the text. But it is difficult to measure the overall improvement in the model fits from this presentation. A better measure is given by

Table 8
Tests of Standard Model Assumptions[a]

Parameter	ΛCDM[b]	ΛCDM+Δ_z[c]	ΛCDM+$Y_{\rm He}$[d]
Fit parameters			
$\Omega_b h^2$	$0.02258^{+0.00057}_{-0.00056}$	0.02244 ± 0.00055	$0.02253^{+0.00056}_{-0.00058}$
$\Omega_c h^2$	0.1109 ± 0.0056	$0.1117^{+0.0054}_{-0.0055}$	$0.1130^{+0.0078}_{-0.0077}$
Ω_Λ	0.734 ± 0.029	0.728 ± 0.028	$0.729^{+0.031}_{-0.032}$
$\Delta^2_{\mathcal{R}}$	$(2.43 \pm 0.11) \times 10^{-9}$	$(2.46 \pm 0.12) \times 10^{-9}$	$(2.43 \pm 0.11) \times 10^{-9}$
n_s	0.963 ± 0.014	$0.958^{+0.013}_{-0.014}$	$0.969^{+0.017}_{-0.018}$
τ	0.088 ± 0.015	0.087 ± 0.015	$0.088^{+0.014}_{-0.015}$
$Y_{\rm He}$	...	...	$0.28^{+0.14}_{-0.15}$
Derived parameters			
t_0	13.75 ± 0.13 Gyr	$13.77^{+0.13}_{-0.12}$ Gyr	13.69 ± 0.16 Gyr
H_0	71.0 ± 2.5 km s^{-1} Mpc^{-1}	70.5 ± 2.4 km s^{-1} Mpc^{-1}	70.9 ± 2.5 km s^{-1} Mpc^{-1}
σ_8	0.801 ± 0.030	0.802 ± 0.030	$0.820^{+0.053}_{-0.054}$

Notes.
[a] Models fit to seven-year *WMAP* data only. See Komatsu et al. (2011) for additional constraints.
[b] Repeated from Table 3 for comparison.
[c] Allows width of reionization to vary. The constraints on Δ_z are limited by the prior $0.5 < \Delta_z < 15$ and so are not listed in the table.
[d] Allows primordial helium mass fraction to vary (cf. $Y_{\rm He}$=0.24).

comparing the allowable volume in N-dimensional parameter space for each of the models.

As a proxy for allowable volume, we compute the square root of the determinant of the parameter covariance matrix for each model, using data from the Markov chains. For example, with the six-parameter ΛCDM model, we compute the 6×6 covariance matrix directly from the chain samples. The allowable volume ratio is defined as the ratio of the square root of the five-year determinant to the corresponding seven-year value. Models with more fit parameters have more rows and columns in their covariance matrix. While this proxy is only proportional to the volume if the parameter distributions are Gaussian, the error in this approximation will be similar for both the five-year and seven-year data sets, so a comparison is still valid.

Table 9 gives the change in allowable parameter-space volume as a ratio of the five-year to seven-year value. These results are based on fits to *WMAP* data only. Overall, the six-parameter ΛCDM model is measured a factor of 1.5 more precisely with the seven-year data while the model with two additional parameters, tensors plus a running spectral index, is measured a factor of three times more precisely. Models with one additional parameter typically improve by factors of 1.8–1.9.

Table 9
Parameter-space Volume Reduction[a]

Model	Dimension	Ratio[b]
ΛCDM (Table 3)	6	1.5
ΛCDM+tensors (Table 4)	7	1.9
ΛCDM+running (Table 4)	7	1.7
ΛCDM+tensors+running (Table 4)	8	3.0
ΛCDM+anti-correlated isocurvature (Table 5)	7	1.9
ΛCDM+uncorrelated isocurvature (Table 5)	7	1.9
ΛCDM+massive neutrinos (Table 3)	7	1.8
oΛCDM (Table 6)	7	1.8
wCDM (Table 6)	7	1.5

Notes.
[a] The relative change in allowable parameter-space volume when models are fit to the seven-year *WMAP* data in place of the five-year data. For a given model, the allowable volume is defined as the square root of the determinant of the parameter covariance matrix, as obtained from the Markov chains. The basic set of six parameters compared in the first row are $\{\Omega_b h^2, \Omega_c h^2, \Omega_\Lambda, \Delta^2_{\mathcal{R}}, n_s, \tau\}$. Additional parameters are as noted in the first column.
[b] The ratio of allowable parameter-space volume: five years over seven years, when fit to *WMAP* data only.

5. GOODNESS OF FIT

Given a best-fit model from the MCMC analysis, we can ask how well the model fits the data. Given that the likelihood function is non-Gaussian, answering the question is not as straightforward as testing the χ^2 per degree of freedom of the best-fit model. Instead we resort to Monte Carlo simulations and compare the absolute likelihood obtained from fitting the flight data to an ensemble of simulated values.

For testing goodness of fit, we generate 500 realizations of the seven-year sky map data that include the CMB signal and instrument noise. These are the same realizations as were used for parameter recovery in Section 3 and are discussed in more detail in Appendix A.

For each realization of a seven-year data set, we constructed the likelihood function appropriate to those data. This required forming the high-l MASTER spectra and the low-resolution sky maps used in the code. (For this study we did not employ Gibbs sampling for the low-l TT likelihood, rather we used a direct pixel-space code that was computationally slower than the Blackwell–Rao estimate per likelihood evaluation, but it required less setup overhead per data realization.) For goodness-of-fit testing, we evaluated the likelihood of the input ΛCDM model for each data realization.

Due to its hybrid nature, the likelihood produces several components that need to be combined to obtain the full likelihood. The components of most interest to goodness-of-fit testing are the high-l TT and TE portions, which cover the bulk of the multipole range and are the most straightforward to interpret. Recall the high-l TT component contains both a Gaussian and a log-normal contribution, as per Equation (11) of Verde et al. (2003)

$$\ln \mathcal{L} = \tfrac{1}{3} \ln \mathcal{L}_{\rm Gauss} + \tfrac{2}{3} \ln \mathcal{L}'_{\rm LN}. \quad (15)$$

Here, the first term can be compared to χ^2, as per Equation (6) of Verde et al. (2003)

$$\ln \mathcal{L}_{\rm Gauss} \propto -\frac{1}{2}\sum_{ll'}\left(\hat{\mathcal{C}}_l - \mathcal{C}_l^{\rm th}\right) Q_{ll'}\left(\hat{\mathcal{C}}_{l'} - \mathcal{C}_{l'}^{\rm th}\right), \qquad (16)$$

where Q is the inverse covariance matrix of the observed power spectrum $\hat{\mathcal{C}}$ and $\mathcal{C}^{\rm th}$ is the model spectrum. The high-l portion of the TE likelihood includes only the Gaussian component, which is a good approximation given the lower signal-to-noise ratio of the TE data. In the following, we report on the distribution of $-2\ln\mathcal{L}$ which we call the effective χ^2.

We compare the distribution of effective χ^2 values for the high-l TT portion of the likelihood, which contains 1170 multipoles from $l = 31$–1200, to a χ^2 distribution with 1170 degrees of freedom. The agreement between the two distributions is good. We tentatively attribute a small shape difference between them to the non-Gaussian component in the likelihood. The effective χ^2 for the seven-year flight TT spectrum is 1227 for 1170 degrees of freedom, after marginalizing over point sources and the SZ spectrum (which are not in the simulations). According to the Monte Carlo distribution, 48/500 of the realizations had a higher effective χ^2, indicating that the flight data are reasonably well fit by the ΛCDM model spectrum.

We perform a similar comparison for the high-l TE data, which covers the multipole range $l = 24$–800. One point of note is that we have adjusted our empirical calibration of $f_{\rm sky,TE}$ as a result of these simulations: the new value is 1.011 times larger than we used in the five-year analysis, which is equivalent to overestimating the five-year TE errors by 1.1%. The recalibrated Monte Carlo distribution tracks the pure χ^2 distribution, consistent with the high-l TE likelihood being Gaussian. The effective χ^2 for the seven-year flight TE spectrum is 807 for 777 degrees of freedom (again, after marginalization over point sources and the SZ spectrum). According to the Monte Carlo distribution, 113/500 of the simulations had a higher effective χ^2, which could easily happen by random chance. This indicates that the ΛCDM theory yields a TE spectrum that fits the data well.

6. CONCLUSIONS

We present the angular power spectra derived from the seven-year *WMAP* sky maps and discuss the cosmological conclusions that can be inferred from *WMAP* data alone.

With the seven-year data, the temperature (TT) spectrum measurement is now limited by cosmic variance for multipoles $l < 548$, and the signal-to-noise ratio per multipole exceeds unity for $l < 919$. In a band power of width $\Delta l = 10$ the signal-to-noise ratio exceeds unity to $l = 1060$. The third acoustic peak in the TT spectrum is now well measured by *WMAP*. In the context of a flat ΛCDM model, this improvement allows us to place tighter constraints on the matter density from *WMAP* data alone, $\Omega_m h^2 = 0.1334^{+0.0056}_{-0.0055}$, and on the epoch of matter-radiation equality, $z_{\rm eq} = 3196^{+134}_{-133}$. The temperature-polarization (TE) spectrum is detected in the seven-year data with a significance of 20σ, compared to 13σ with the five-year data. We now detect the second dip in the TE spectrum near $l \sim 450$ with high confidence. The TB and EB spectra remain consistent with zero in the seven-year data. This demonstrates low systematic errors in the data and is used to place 33% tighter limits on the rotation of linear polarization due to parity-violating effects: $\Delta\alpha = -1.^\circ1 \pm 1.^\circ4({\rm stat.}) \pm 1.^\circ5({\rm sys.})$ (Komatsu et al. 2011). The low-l EE spectrum, a measure of the optical depth due to reionization, is detected at 5.5σ significance when averaged over $l = 2$–7: $l(l+1)C_l^{\rm EE}/(2\pi) = 0.074^{+0.034}_{-0.025}\,\mu{\rm K}^2$ (68% CL). The high-l EE spectrum in the range $24 \leqslant l \leqslant 800$ is detected at over 8σ. The BB spectrum, an important probe of gravitational waves from inflation, remains consistent with zero; when averaged over $l = 2$–7, $l(l+1)C_l^{\rm BB}/(2\pi) < 0.055\,\mu{\rm K}^2$ (95% CL). The upper limit on tensor modes from polarization data alone is a factor of two lower with the seven-year data than it was using the five-year data (Komatsu et al. 2011).

The data remain consistent with the simple ΛCDM model. The best-fit ΛCDM parameter values are given in Table 3; the TT spectrum from this fit has an effective χ^2 of 1227 for 1170 degrees of freedom, with a probability to exceed of 9.6%. The allowable volume in the six-dimensional space of ΛCDM parameters has been reduced by a factor of 1.5 relative to the five-year volume. Most models with one additional parameter beyond ΛCDM see volume reduction factors of 1.8–1.9, while the ΛCDM model that allows for tensor modes and a running scalar spectral index has a factor of three lower volume when fit to the seven-year data. We test the parameter recovery process for bias and find that the scalar spectral index, n_s, is biased high, but only by 0.09σ, while the remaining parameters are biased by $<0.15\sigma$.

The improvement in the third peak measurement leads to tighter lower limits from *WMAP* on the number of relativistic degrees of freedom (e.g., neutrinos) in the early universe: $N_{\rm eff} > 2.7$ (95% CL). Also, using *WMAP* data alone, the primordial helium mass fraction is found to be $Y_{\rm He} = 0.28^{+0.14}_{-0.15}$, and with data from higher-resolution CMB experiments included, Komatsu et al. (2011) establish the existence of pre-stellar helium at $> 3\sigma$.

The *WMAP* mission is made possible by the support of the NASA Science Mission Directorate. This research has made use of NASA's Astrophysics Data System Bibliographic Services. Some of the results in this paper have been derived using the HEALPix (Gorski et al. 2005) package. We acknowledge use of the CAMB (Lewis et al. 2000) and CMBFAST (Seljak & Zaldarriaga 1996) packages.

APPENDIX A

PARAMETER RECOVERY SIMULATIONS

This appendix describes the configuration of the set of 500 simulations that was used for checking parameter recovery and the χ^2 values from the likelihood.

The mask is the KQ85y7 mask, which lets through 78.3% of the sky.

For instrument noise, we employ a two-step process in which we generate uncorrelated noise at high resolution and combine it with low-resolution correlated noise. The noise was constructed from the seven-year $N_{\rm side} = 512$ and 1024 $N_{\rm obs}$ maps, the seven-year $N_{\rm side} = 16$ covariance matrices, the seven-year σ_0 values, and the seven-year synchrotron cleaning factors, given in Gold et al. (2011). For each year and nine DAs (Ka1–W4), a high-resolution uncorrelated noise map was made with I, Q, and U components at $N_{\rm side} = 512$ and 1024, including the QU correlations within each pixel. The noise maps are generated on a single-year, single-DA basis so we can mimic the construction of the flight spectra and likelihood function. A correlated noise map was made at $N_{\rm side} = 16$. The σ_0 values

for the polarization portion of these maps were increased by a factor of $1/(1-a_1)$, where a_1 is the fraction of the K-band map which has been removed to avoid synchrotron contamination (Gold et al. 2011). This accounts for the increased noise due to the synchrotron template subtraction. We combined the low-resolution ($N_{\rm side} = 16$) and high-resolution ($N_{\rm side} = 512$ or 1024) maps by subtracting off the mean of the high-resolution noise within each low-resolution pixel, and then added the low-resolution noise to all high-resolution pixels within that low-resolution pixel. This process provides a high-resolution noise realization that has the proper low-resolution noise correlations when it is binned. Note that the $N_{\rm side} = 512$ and 1024 maps have different noise realizations, but this will have no effect on the resultant likelihoods, because the $N_{\rm side} = 512$ maps are used for polarization and the $N_{\rm side} = 1024$ maps are used for temperature, following the procedure used in the standard *WMAP* pipeline.

The CMB signal is assumed to be Gaussian, and random-phase, and so its statistical properties are completely defined by a power spectrum. The parameter recovery simulations all use the same power spectrum, which was derived from the best fit to a five-year ΛCDM Markov chain, with *WMAP*, BAO, and Supernova data. The parameters used are $\Omega_b h^2 = 0.0022622$, $\Omega_c h^2 = 0.1138$, $H_0 = 70.234$ km s^{-1}Mpc^{-1}, $\Delta^2_{\mathcal{R}} = 2.4588 \times 10^{-9}$, $n_s = 0.9616$, and $\tau = 0.08785$. The gravitational lensing signal is treated as Gaussian, and the effects on the temperature and polarization power spectra are included. However, the BB spectrum has been zeroed, for consistency with a map-making simulation done previously. Zeroing the BB spectrum will have no effect on parameter recovery, since our simple ΛCDM model has a tensor to scalar ratio of 0, and therefore an undetectable BB spectrum. Each CMB realization has the same theoretical power spectrum, but different cosmic variance. The different DAs in a given realization all see the same CMB sky, but with different smoothing, and different noise. The smoothing used for each DA is a circular beam response based on the appropriate seven-year beam transfer function (Jarosik et al. 2011).

These simulations do not include foregrounds, the Sunyaev–Zel'dovich effect, unresolved point sources, or beam uncertainty.

The analysis of the parameter recovery simulations uses the same parameters as went into the maps, in the case of $N_{\rm obs}$, beam profiles, and usage of gravitational lensing. However, for the σ_0 and synchrotron cleaning coefficients, the simulations were produced with the seven-year values and analyzed with the previous five-year values. Note that this is a small difference, because the seven-year values are not very different from the five-year values.

The parameter recovery importance sampling used the 2008 September version of CAMB, and so does not include the bug fix for the proton mass error. This has no effect on the simple ΛCDM model explored here.

APPENDIX B

RECFAST AND *WMAP* LIKELIHOOD UPDATES

As mentioned in Section 2.6, since the original version of this paper, there have been two updates to the parameter estimation code: an improvement in RECFAST from version 1.4.2 to version 1.5, which includes an improved model of the hydrogen atom; and a small bug fix in the *WMAP* likelihood code, changing its version from 4.0 to 4.1.

Table 10
Likelihood Updates[a]

Parameter	Updated[b]	Original[c]
Fit parameters		
$10^2\Omega_b h^2$	$2.249^{+0.056}_{-0.057}$	$2.258^{+0.057}_{-0.056}$
$\Omega_c h^2$	0.1120 ± 0.0056	0.1109 ± 0.0056
Ω_Λ	$0.727^{+0.030}_{-0.029}$	0.734 ± 0.029
$\Delta^2_{\mathcal{R}}$	$(2.43 \pm 0.11) \times 10^{-9}$	$(2.43 \pm 0.11) \times 10^{-9}$
n_s	0.967 ± 0.014	0.963 ± 0.014
τ	0.088 ± 0.015	0.088 ± 0.015
Derived parameters		
t_0	13.77 ± 0.13 Gyr	13.75 ± 0.13 Gyr
H_0	70.4 ± 2.5 km s^{-1} Mpc^{-1}	71.0 ± 2.5 km s^{-1} Mpc^{-1}
σ_8	$0.811^{+0.030}_{-0.031}$	0.801 ± 0.030
Ω_b	0.0455 ± 0.0028	0.0449 ± 0.0028
Ω_c	0.228 ± 0.027	0.222 ± 0.026
$z_{\rm reion}$	10.6 ± 1.2	10.5 ± 1.2

Notes.

[a] Seven-year ΛCDM parameters, to illustrate the differences between two versions of RECFAST and two versions of the likelihood code. The six-parameter model and priors are the same as previously used in Sections 3 and 4 and mentioned in Table 3. Here, we also marginalize over the SZ effect, as in Section 4.1.

[b] The updated version of the parameters, based on RECFAST 1.5 and version 4.1 of the *WMAP* likelihood. This version is more accurate, but was not available when the chains in the rest of this paper were run.

[c] The original version of the parameters, based on RECFAST 1.4.2 and version 4.0 of the *WMAP* likelihood. This is the code configuration used for the chains reported in this paper.

We have rerun the ΛCDM parameter fits using the version 4.1 likelihood, and find parameter changes of order 0.1σ. The effect on parameters of updating to the new version of RECFAST in CAMB is also of order 0.1σ. The largest combined changes are an increase in σ_8 of 0.35σ, and an increase in the spectral index n_s of 0.26σ; Table 10 provides more detailed information on several original and updated parameter values.

REFERENCES

Bean, R., Dunkley, J., & Pierpaoli, E. 2006, Phys. Rev. D, 74, 063503
Bennett, C. L., et al. 2003a, ApJS, 148, 1
Bennett, C. L., et al. 2003b, ApJ, 583, 1
Bennett, C. L., et al. 2011, ApJS, 192, 17
Bond, J. R., Jaffe, A. H., & Knox, L. 1998, Phys. Rev. D, 57, 2117
Brown, M. L., et al. 2009, ApJ, 705, 978
Chu, M., Eriksen, H. K., Knox, L., Górski, K. M., Jewell, J. B., Larson, D. L., O'Dwyer, I. J., & Wandelt, B. D. 2005, Phys. Rev. D, 71, 103002
Colombo, L. P. L., & Pierpaoli, E. 2010, MNRAS, 407, 247
Dunkley, J., et al. 2009, ApJS, 180, 306
Eriksen, H. K., et al. 2004, ApJS, 155, 227
Eriksen, H. K., et al. 2007, ApJ, 656, 641
Fukugita, M., & Kawasaki, M. 2006, ApJ, 646, 691
Gold, B., et al. 2009, ApJS, 180, 265
Gold, B., et al. 2011, ApJS, 192, 15
Goldberg, J. N., MacFarlane, A. J., Newman, E. T., Rohrlich, F., & Sudarshan, E. C. G. 1967, J. Math. Phys., 8, 2155
Gorski, K. M., Hivon, E., Banday, A. J., Wandelt, B. D., Hansen, F. K., Reinecke, M., & Bartlemann, M. 2005, ApJ, 622, 759
Gruenwald, R., Steigman, G., & Viegas, S. M. 2002, ApJ, 567, 931
Gruppuso, A., de Rosa, A., Cabella, P., Paci, F., Finelli, F., Natoli, P., de Gasperis, G., & Mandolesi, N. 2009, MNRAS, 400, 463
Hinshaw, G., et al. 2003, ApJS, 148, 135
Hinshaw, G., et al. 2007, ApJS, 170, 288
Hivon, E., Górski, K. M., Netterfield, C. B., Crill, B. P., Prunet, S., & Hansen, F. 2002, ApJ, 567, 2
Ichikawa, K., Fukugita, M., & Kawasaki, M. 2005, Phys. Rev. D, 71, 043001
Izotov, Y. I., & Thuan, T. X. 2004, ApJ, 602, 200
Jarosik, N., et al. 2011, ApJS, 192, 14
Jewell, J., Levin, S., & Anderson, C. H. 2004, ApJ, 609, 1

Jewell, J. B., Eriksen, H. K., Wandelt, B. D., O'Dwyer, I. J., Huey, G., & Górski, K. M. 2009, ApJ, 697, 258
Kamionkowski, M., Kosowsky, A., & Stebbins, A. 1997, Phys. Rev. D, 55, 7368
Komatsu, E., & Seljak, U. 2002, MNRAS, 336, 1256
Komatsu, E., et al. 2003, ApJS, 148, 119
Komatsu, E., et al. 2009, ApJS, 180, 330
Komatsu, E., et al. 2011, ApJS, 192, 18
Kosowsky, A., & Turner, M. S. 1995, Phys. Rev. D, 52, 1739
Larson, D. L. 2006, PhD thesis, Univ. Illinois at Urbana–Champaign
Lewis, A. 2008, Phys. Rev. D, 78, 023002
Lewis, A., Challinor, A., & Lasenby, A. 2000, ApJ, 538, 473
Mackay, D. 2003, Information Theory, Inference, and Learning Algorithms (Cambridge: Cambridge Univ. Press)
Newman, E. T., & Penrose, R. 1966, J. Math. Phys., 7, 863
Nolta, M. R., et al. 2009, ApJS, 180, 296
O'Dwyer, I. J., et al. 2004, ApJ, 617, L99
Olive, K. A., & Skillman, E. D. 2004, ApJ, 617, 29
Page, L., et al. 2007, ApJS, 170, 335
Peimbert, M., Luridiana, V., & Peimbert, A. 2007, ApJ, 666, 636
Riess, A. G., et al. 2009, ApJ, 699, 539
Rudjord, Ø., Groeneboom, N. E., Eriksen, H. K., Huey, G., Górski, K. M., & Jewell, J. B. 2009, ApJ, 692, 1669
Scott, D., & Moss, A. 2009, MNRAS, 397, 445
Seager, S., Sasselov, D. D., & Scott, D. 1999, ApJ, 523, L1
Seager, S., Sasselov, D. D., & Scott, D. 2000, ApJS, 128, 407
Seljak, U., & Zaldarriaga, M. 1996, ApJ, 469, 437
Spergel, D. N., et al. 2003, ApJS, 148, 175
Spergel, D. N., et al. 2007, ApJS, 170, 377
Steigman, G. 2007, Annu. Rev. Nucl. Part. Sci., 57, 463
Verde, L., et al. 2003, ApJS, 148, 195
Wandelt, B. D., Larson, D. L., & Lakshminarayanan, A. 2004, Phys. Rev. D, 70, 083511
Weiland, J. L., et al. 2011, ApJS, 192, 19
Wong, W. Y., Moss, A., & Scott, D. 2008, MNRAS, 386, 1023
Zaldarriaga, M., & Seljak, U. 1997, Phys. Rev. D, 55, 1830